

1
2
3
4
5
6
7
8
9
10
11
12
13
14
15
16
17
18
19
20
21
22
23
24
25
26
27
28
29
30
31
32
33
34
35
36
37
38
39
40
41
42
43
44
45
46
47
48
49
50
51
52
53
54
55
56
57
58
59
60
61
62
63
64
65

Noname manuscript No. (will be inserted by the editor)

Examining the limits of cellular adaptation bursting mechanisms in biologically-based excitatory networks of the hippocampus

K.A. Ferguson¹, F. Njap¹, W. Nicola¹, F.K. Skinner²,
S.A. Campbell²

Received: date / Accepted: date

Abstract Determining the biological details and mechanisms that are essential for the generation of population rhythms in the mammalian brain is a challenging problem. This problem cannot be addressed either by experimental or computational studies in isolation. Here we show that computational models that are carefully linked with experiment provides insight into this problem. Using the experimental context of a whole hippocampus preparation *in vitro* that spontaneously expresses theta frequency (3-12 Hz) population bursts in the CA1 region, we create excitatory network models to examine whether cellular adaptation bursting mechanisms could critically contribute to the generation of this rhythm. We use biologically-based cellular models of CA1 pyramidal cells and network sizes and connectivities that correspond to the experimental context. By expanding our mean field analyses to networks with heterogeneity and non all-to-all coupling, we allow closer correspondence with experiment, and use these analyses to greatly extend the range of parameter values that are explored. We find that our model excitatory networks can produce theta frequency population bursts in a robust fashion. Thus, even though our networks are limited by not including inhibition at present, our results indicate that cellular adaptation in pyramidal cells could be an important aspect for the occurrence of theta frequency population bursting in the hippocampus. These models serve as a starting framework for the inclusion of inhibitory cells and for the consideration of additional experimental features not captured in our present network models.

Keywords mean field theory, network model, theta rhythm, mathematical model

This work was supported by NSERC Canada.

¹Shared First Authors

²Shared Senior Authors

KAF, FN, FKS
TWRI/UHN, KDT, 60 Leonard Ave., Toronto Ontario M5T 2S8
E-mail: frances.skinner@gmail.com

FN, WN, SAC
Department of Applied Mathematics, University of Waterloo
E-mail: sacampbell@uwaterloo.ca

1 Introduction

The emergent behaviour in networks of neurons depends on the characteristics of the individual neurons, their connectivity profile and properties, as well as the size of the network. Theoretical and modeling studies have shown that population bursts can emerge from networks of neurons that are coupled with excitatory synapses, when the isolated neurons themselves do not burst, but do express spike frequency adaptation (Gutkin and Zeldenrust, 2014). In this situation it has been shown that network bursting arises if there is an appropriate balance between excitatory drive and the amount of spike frequency adaptation (Dur-E-Ahmad et al, 2011; Latham et al, 2000; van Vreeswijk and Hansel, 2001). **Emergent network bursting can also occur if other slow processes are present either internal to the cell (Butera et al, 1999b) or in the synapses (Tabak et al, 2000; Vladimirovski et al, 2008).**

The hippocampus is a major communication hub for memory processing (Battaglia et al, 2011) via its expression of population activities that include sharp wave and theta frequency bursting (Buzsaki, 2011). Bursting activity is thought to be important for synaptic plasticity and brain coding mechanisms (Lisman, 1997). However, it is not clearly known how population bursts in hippocampus emerge in order to play their essential communication roles with other brain regions. That is, what mechanisms underlie this emergence? Do cellular-based adaptation mechanisms contribute to this emergence in the hippocampus?

There are many biological details that might be important in the generation of population bursts in the hippocampus. However, what the essential balances and mechanisms may be are challenging to determine and cannot be extracted from experimental studies on their own. To determine whether cellular adaptation mechanisms are important in the production of population bursts in the hippocampus, we link experimental, modeling and theoretical studies. It is clear that one cannot ignore cellular details in understanding network dynamics (Skinner, 2012), and at the same time, there are many synaptic details that may play important roles (e.g., see Tóth (2010)). As such, the interpretation of model parameters and links to experiments require careful consideration. In this work, we take a balanced approach in which network size, cellular and connectivity properties are designed to have biological linkages in a context of hippocampal theta (3-12 Hz) population bursts. Even though these linkages are (by necessity) limited, we clearly express the rationale and limitations so that they can serve as a foundation for future studies. **In the present work, we limit our considerations to networks in the absence of inhibition. In this way, we can determine whether cellular adaptation mechanisms in excitatory networks alone are able to contribute to theta frequency population bursting.**

Our work is based on a whole hippocampus preparation that spontaneously expresses population, theta rhythms (Goutagny et al, 2009), and we use previously developed biologically-based cellular models of excitatory cells (Ferguson et al, 2015). Several thousands of excitatory cells are involved and thus fully exploring the model parameter space would be challenging, even with our simplified cellular representations. We therefore develop theoretical mean-field analyses to efficiently explore the parameter space. We focus on area CA1 of the hippocampus where these theta rhythms occur and here, the excitatory cells are minimally coupled. Due to the close correspondence between the mean-field analyses and the full simulations, it is possible to explore a very wide range of parameter balances using the mean-field analyses, and the parameter regimes which then need to be explored with full simulations are much reduced. In this way, we are able to significantly constrain the

parameter regimes for which population bursts could occur in large, excitatory networks of the hippocampus. We find that robust, theta frequency population bursts can occur in our biologically-based cellular **excitatory** networks using physiologically reasonable synaptic conductance strengths, time constants and connectivities. This suggests that cellular adaptation mechanisms **in excitatory networks could critically contribute to the generation of theta bursts in the hippocampus. Our present models do not include inhibition and so it is not surprising that they are not able to capture all features of the experimental data such as sparse firing. At this stage, we view our excitatory, pyramidal cell networks as setting an experimentally-constrained starting framework on which we can build.** Our work can be considered as a way to examine and determine mechanisms that are in play in biological systems. That is, an intertwining of theoretical, modeling and experimental aspects carried out at initial stages.

2 Methods

2.1 Experimental context and network size

An intact, whole hippocampus *in vitro* rodent preparation that expresses theta rhythms (3-12 Hz) has been developed (Goutagny et al, 2009). By blocking synaptic transmission in different regions, the minimum circuitry required to independently generate theta rhythms in this preparation is estimated to be about a 1 mm^3 volume of tissue in the CA1 region of the hippocampus. For this volume of tissue, there are approximately 30,000 excitatory, pyramidal cells (Bezaire and Soltesz, 2013), as well as thousands of **inhibitory cells of many different types**. CA1 pyramidal cells are connected to each other, but the connectivity is minimal (Deuchars and Thomson, 1996), estimated to be on the order of 1% or less (Bezaire and Soltesz, 2013).

2.2 Cellular and network models

For the mathematical model of an excitatory, pyramidal cell of CA1 hippocampus, we use our previously developed model which is based on experimental data from the *in vitro* whole hippocampus preparation. The details underlying the rationale and development of our pyramidal cell models are given in Ferguson et al (2015). Briefly, the experimental data showed clear evidence of spike frequency adaptation in recordings from CA1 pyramidal cells when synaptic activity was blocked, and this adaptation could be strong or weak. **Intrinsically bursting neurons were not observed in the limited experimental datasets.** It is interesting to note that different amounts of adaptation have also been found in CA3 pyramidal cells (Hemond et al, 2008). We captured the spike frequency adaptation in our models by doing ad-hoc fits to the experimental frequency-current (f-I) curves which show both initial and steady state frequency. As such, we consider our cellular models to be biologically-based, but not biophysically-based, as they do not include voltage-gated channels.

The cellular-based network model structure is given below. The cellular model is based on that developed by Izhikevich (Izhikevich, 2003). It captures the subthreshold behaviour and the upstroke of the action potential, and uses a reset mechanism to represent the spike's fast downstroke. An important advantage of this model is that it is relatively simple, but still allows us to choose parameters that have a well-defined (albeit limited) relationship to the electrophysiological recordings. It has a fast variable representing the membrane potential, V (mV), and a variable for the slow

recovery current, u (pA). We used a slight modification to be able to reproduce the spike width. The model is given by:

$$\begin{aligned} C_m \dot{V} &= k(V - v_r)(V - v_t) - u + I_{applied} + I_{shift} - I_{syn} \\ \dot{u} &= a[b(V - v_r) - u] \end{aligned} \quad (1)$$

$$\begin{aligned} &\text{if } V \geq v_{peak}, \text{ then } V \leftarrow c, u \leftarrow u + d \\ &\text{where } k = k_{low} \text{ if } V \leq v_t, k = k_{high} \text{ if } V > v_t \end{aligned}$$

The parameters are as follows:

C_m (pF) is the membrane capacitance.

v_r (mV) is the resting membrane potential.

v_t (mV) is the instantaneous threshold potential.

v_{peak} (mV) is the spike cut-off value.

$I_{applied}$ (pA) is the applied current, and represents all synaptic input to the cells that is not directly modelled through I_{syn} .

I_{shift} (pA) is a current that shifts the f-I curve laterally to allow the model to easily capture the rheobase current (for the strongly/weakly adapting models, rheobase current is 0/5 pA respectively).

I_{syn} (pA) represents the synaptic input from the presynaptic cell population (further details below).

a (ms^{-1}) is the recovery time constant of the adaptation current.

b (nS) describes the sensitivity of the adaptation current to subthreshold fluctuations. Greater values couple V and u more strongly resulting in possible subthreshold oscillations and low-threshold spiking dynamics.

c (mV) is the voltage reset value.

d (pA) is the total amount of outward minus inward currents activated during the spike and affecting the after-spike behaviour.

k (nS/mV) represents a scaling factor.

The parameters v_r , v_t , v_{peak} , and c were directly based on the intrinsic spike characteristics derived from the recordings. k_{high} was determined such that the width of the action potential from threshold in the model matched the average spike width at threshold in the biological cells. The adaptation parameters a and d were determined such that the model produced the amount of adaptation observed experimentally. The parameters b and k_{low} were varied systematically to determine values in which the slope of the model f-I curve was within the range of slopes determined from the experimental f-I curves. Further details can be found in Ferguson et al (2015). Parameter values for the strongly and weakly adapting pyramidal cell models are given in Table 1. **For these parameter values the model can only exhibit two types of behaviour, quiescence and tonic spiking, depending on whether $I_{applied}$ is above or below rheobase. Thus, any bursting observed is an emergent network phenomenon.**

Synaptic input is modelled through a chemical synapse represented by:

$$I_{syn} = gs(V - E_{rev}) \quad (2)$$

where g (nS) is the maximal synaptic conductance of the synapse from a presynaptic neuron to the postsynaptic neuron, E_{rev} is the reversal potential of the synapse, and V is the membrane potential

of the postsynaptic cell. The gating variable, s , represents the fraction of open synaptic channels, and is given by first order kinetics (Destexhe et al (1994), and see p.159 in Ermentrout and Terman (2010)):

$$\dot{s} = \alpha[T](1 - s) - \beta s \quad (3)$$

The parameters α (in $mM^{-1}ms^{-1}$) and β (in ms^{-1}) in Equation 3 are related to the inverse of the rise and decay time constants (τ_R , τ_D in ms). $[T]$ represents the concentration of transmitter released by a presynaptic spike. Suppose that the time of a spike is $t = t_0$ and $[T]$ is given by a square pulse of height $1 mM$ lasting for $1 ms$ (until t_1). Then, we can represent

$$s(t - t_0) = s_\infty + (s(t_0) - s_\infty)e^{-\frac{t-t_0}{\tau_s}}, \quad t_0 < t < t_1$$

where

$$s_\infty = \frac{\alpha}{\alpha + \beta} \text{ and } \tau_s = \frac{1}{\alpha + \beta} \quad (4)$$

After the pulse of transmitter has gone, $s(t)$ decays as

$$s(t) = s(t_1)e^{-\beta(t-t_1)} \quad (5)$$

While we explicitly model the synaptic input through Equation 2, we represent the synaptic input that is not explicitly modelled through an applied current ($I_{applied}$). These applied currents (in pA) are constant, tonic input to individual cells (usually heterogeneous across cells, such that the input is normally distributed with a mean of $I_{applied}$ and a standard deviation of σ_I).

2.3 Paper focus and experimental constraints

While there are, of course, both excitatory and inhibitory cells in hippocampal neuronal networks, we only consider excitatory networks. This allows us to focus on the extent to which it is possible to obtain population bursting in such models when there are experimental constraints on network size, connectivity and connection strengths. Furthermore, in the experiments on which our constraints are based, the theta rhythm is much more dependent on excitatory AMPA/kainate, compared with NMDA glutamatergic synapses, since theta power is essentially diminished when AMPA/kainate receptor blockers are applied but unaffected when NMDA receptor blockers are used (Goutagny et al, 2009). Thus, our focus is on excitatory, pyramidal cell networks connected with AMPA synapses, and for our simulations, we use the following terminology for the synaptic currents:

$$I_{syn} = g_{pyr}s_{pyr}(V - E_{pyr}) \quad (6)$$

where g_{pyr} (nS) is the maximal synaptic conductance of the recurrent excitatory synapses, the gating variable, s_{pyr} , represents the fraction of open synaptic channels, and E_{pyr} (mV) is the excitatory, pyramidal reversal potential.

Experimentally, it was determined that excitatory postsynaptic currents reversed around $-15 mV$ (junction potential corrected) (Huh et al, 2015). The rise and decay time constants are taken to be $\tau_R = 0.5 ms$ and $\tau_D = 3 ms$ respectively, based on Spruston et al (1995). Given that a single, excitatory AMPA channel has a conductance of 8-10 pS and that there are 300-500 channels per synaptic connection (Spruston et al, 1995; Tóth, 2010), the maximum, possible range for biological synaptic conductance strengths (g_{pyr}) is thus 0.008-5 nS.

2.4 Model simulations and analyses

The network simulations were done using the Brian simulator (Goodman and Brette, 2009), and custom python code was written for the analyses. The computing platform used is the GPC supercomputer at the SciNet High Performance Computing Consortium (Loken et al, 2010) (<http://www.scinethpc.ca/>). The initial conditions of our membrane potentials (V) are chosen to be uniform random values from -55 to -65 mV , and the other variables (u 's and s 's were set at 0). We use the forward Euler method for integration with a time step of 0.02 ms .

Simulations with networks of different sizes (1,000 to 30,000 cells) are done. The networks are heterogeneous in that each cell receives a different input, with mean $I_{applied}$ and variance σ_I , as chosen from a normal distribution. Several of the network simulations are further analyzed by determining a number of features about the network. We first determine our population burst by plotting the (normalized) spike time distribution, using a bin width of 10 ms. We use a defined threshold of 0.15 and the burst duration time would then be considered the time between the upstroke and the downstroke considering this threshold of the distribution. We use a fixed threshold to ensure a comparable criteria in our burst definition. In this way, we obtain (population) burst durations (i.e., burst widths) and interburst durations, and burst periods (sum of burst duration and interburst duration). From this, we further compute spiking frequencies, number of spiking cells and number of spikes per cell during the bursts (intraburst) and between the bursts (interburst).

2.5 Theoretical mean-field analyses

We develop a mean-field model which consists of a three dimensional system of non-smooth ordinary differential equations. This model is used to predict regions in parameter space where bursting with specific frequencies occurs. Our model is based on a population density approach and a reduction due to time scale separation.

We have used this approach in various contexts: we have derived mean-field models for both homogeneous (Nicola and Campbell, 2013a) and heterogeneous networks (Nicola and Campbell, 2013b) and in the presence of noise (Nicola et al, 2014). In these papers, the neural models were of the same type as the one we consider here: two dimensional integrate-and-fire models (Izhikevich, 2003; Brette and Gerstner, 2005; Touboul, 2008). Further, the synaptic connections were modelled using pulse coupling, and the coupling was all-to-all.

In this paper, we extend our derivation to deal with several complications which appear in the model described in the previous section: a slightly more complex neural model due to the switching of the parameter k in Eq. (1), the kinetic-based synapse model given in Eq. (3), and minimal connectivity as opposed to all-to-all coupling.

We briefly review the derivation of mean-field model in the case of all-to-all coupling, the linear double exponential synapse model (Ermentrout and Terman, 2010) and heterogeneity in the applied current and maximal synaptic conductance. Modifications to deal with the kinetic synapse model and the minimal connectivity will be dealt with in the Results section.

The network model in this case, with the cellular model from the previous subsection is

$$V_i' = \frac{1}{C_m} [F(V_i) - u_i + I_i - g_i s_i (V_i - E_{pyr})] = G(V_i, u_i, s_i; I_i, g_i) \quad (7)$$

$$u_i' = a[b(V_i - v_r) - u_i] \quad (8)$$

$$s_i' = -\frac{s_i}{\tau_R} + h_i \quad (9)$$

$$h_i' = -\frac{h_i}{\tau_D} + \frac{A}{N\tau_D\tau_R} \sum_{j=1}^N \sum_{k:t_{j,k} < t} \delta(t - t_{j,k}) \quad (10)$$

where there are jumps as defined in Eq. (1), N is the network size, and A determines the magnitude of the synaptic response. Further, g_i is the maximal synaptic conductance into neuron i . **The double exponential synapse model, eqs. (9)-(10), is two dimensional to allow for different time constants for the rise time (τ_R) and decay time (τ_D) of the synaptic response.** The variable s_i is the average synaptic input to neuron i :

$$s_i(t) = \frac{1}{N} \sum_{j=1}^N s_{ij}(t),$$

and h_i is the corresponding auxiliary synaptic variable. The equations for s_i and h_i follow from those for the individual synapses, s_{ij}, h_{ij} , since the synapse model is linear. Note that, to simplify the notation in the following, we have dropped the subscript *applied* on the input current and *pyr* on the synaptic conductance. We further note that the $I_{shif t}$ term has been absorbed into the $I_{applied}$ term for simplicity.

One aspect of the model developed in the previous section that has not been dealt with in our prior work, is the voltage dependent switching of the parameter k (see Eq. (1)). This is easily taken care of by assuming that k is a function of V_i , i.e.,

$$F(V_i) = k(V_i)(V_i - v_r)(V_i - v_t).$$

This will not change any of our equations, but needs to be taken into account when the expressions are evaluated numerically.

In the population density approach, the behaviour of individual neurons in a network is not tracked. Instead we study the time evolution of a probability density function (pdf) which represents the probability that any individual neuron in the network is in a particular state, or, equivalently, the proportion of neurons in the network that have a particular state (Abbott and van Vreeswijk, 1993; Apfalter et al, 2006; Hansel and Mato, 2001, 2003; Knight, 2000; Ly and Tranchina, 2007).

Let $\rho(V, u, t; I, g)$ be the probability density function for the network (7)-(9). Since the number of neurons in the network is fixed, the pdf must satisfy a continuity partial differential equation (PDE). Supplementing this PDE with differential equations describing the time evolution of the network mean values of s_i and h_i gives a full system of equations for the network.

As shown in Nicola and Campbell (2013b), rewriting the density using conditional probabilities and applying a first order moment closure assumption leads to the following model

$$\begin{aligned} \frac{\partial \rho_V(V, t; I, g)}{\partial t} &= - \frac{\partial J(V, \langle u \rangle, \langle s \rangle, t; I, g)}{\partial V} \\ \langle u \rangle' &= a[b(\langle V \rangle - v_r) - \langle u \rangle] + d \int_I \int_g J(v_{peak}, \langle u \rangle, \langle s \rangle, t; I, g) dg dI \\ \langle s \rangle' &= - \frac{\langle s \rangle}{\tau_R} + \langle h \rangle \\ \langle h \rangle' &= - \frac{\langle h \rangle}{\tau_D} + \frac{A}{\tau_R \tau_D} \int_I \int_g J(v_{peak}, \langle u \rangle, \langle s \rangle, t; I, g) dg dI \end{aligned}$$

where ρ_V is the marginal density of V and J is a flux defined by

$$J(V, \langle u \rangle, \langle s \rangle, t; I, g) = G(V, \langle u \rangle, \langle s \rangle; I, g) \rho_V(V, t; I, g).$$

Assuming that the time scales of the adaption and the synapse are longer than that of the voltage ($\frac{1}{a}, \tau_R, \tau_D \gg 1$), one can apply a quasi-steady state approximation to the PDE to obtain an expression for the density ρ_V and hence the flux, J . Using this in the equations for $\langle u \rangle, \langle s \rangle, \langle h \rangle$ gives the mean-field model

$$\langle u \rangle' = a[b(\langle V \rangle - v_r) - \langle u \rangle] + d \langle R_i(t) \rangle \quad (11)$$

$$\langle s \rangle' = - \frac{\langle s \rangle}{\tau_R} + \langle h \rangle \quad (12)$$

$$\langle h \rangle' = - \frac{\langle h \rangle}{\tau_D} + \frac{A}{\tau_R \tau_D} \langle R_i(t) \rangle \quad (13)$$

where

$$\langle R_i(t) \rangle = \int_I \int_g \langle R_i(t) | I, g \rangle \rho_g(g) \rho_I(I) dg dI \quad (14)$$

$$\langle R_i(t) | I, g \rangle = \begin{cases} \left[\int_{v_{reset}}^{v_{peak}} \frac{C_m}{k(V)(V-v_r)(V-v_t) - \langle u \rangle - g \langle s \rangle (V - E_{pyr}) + I} dV \right]^{-1} & I > I^*(\langle u \rangle, \langle s \rangle, g) \\ 0 & I \leq I^*(\langle u \rangle, \langle s \rangle, g) \end{cases} \quad (15)$$

and

$$I^*(\langle u \rangle, \langle s \rangle, g) = \max_V [-k(V)(V - v_r)(V - v_t) + \langle u \rangle + g \langle s \rangle (V - E_{pyr})]. \quad (16)$$

In later sections we will use the mean firing rate in the more compact form

$$\langle R_i(t) \rangle = \int_g \rho_g(g) \int_{I^*(\langle u \rangle, \langle s \rangle, g)}^{\infty} \rho_I(I) \left[\int_{v_{reset}}^{v_{peak}} \frac{C_m}{k(V)(V - v_r)(V - v_t) - \langle u \rangle - g \langle s \rangle (V - E_{pyr}) + I} dV \right]^{-1} dI dg$$

Our application of the mean-field models in this paper is similar to our previous work (Nicola and Campbell, 2013a,b). As shown in that work, the transition from tonic firing to bursting in

these networks is associated with the emergence of a **limit cycle** in the mean-field model. That is, bursting solutions in the full network model correspond to periodic solutions in the mean-field model. We thus predict the frequency of bursting in the network by determining the period of the limit cycle in the mean-field model. This is done numerically in Matlab by computing the reciprocal of the mean peak to peak time after transients are eliminated. The peak to peak time is computed using the PeakFinder algorithm (Yoder, 2014) from the Matlab file exchange. Our method can only determine the frequency if there are four or more peaks (bursts) during the simulation, thus any simulation with fewer than four peaks is classified as nonbursting. As our standard simulation time was 3 seconds, any simulations with a burst frequency less than about 1.3 Hz is classified as nonbursting.

Code for the mean-field analyses and network simulations will be available online. Pyramidal cell models are available online via <http://modeldb.yale.edu/182515> or <http://www.opensourcebrain.org/projects/ca1-pyr-cell-ferguson-et-al-2014>.

3 Results

From modeling and theoretical studies, it has been shown that one can obtain population bursting in recurrently connected, excitatory networks in which cellular adaptation is present (Dur-E-Ahmad et al, 2011; Latham et al, 2000; van Vreeswijk and Hansel, 2001). The underlying mechanism relies on a balance between the amount of cellular adaptation and excitatory coupling. However, whether cellular adaptation features are sufficient to generate population bursts in biological systems is unclear. Previously, we built excitatory, pyramidal models that had spike adaptation characteristics as observed experimentally in the CA3 region of the hippocampus (Dur-E-Ahmad et al, 2011). However, that work estimated adaptation features from the literature and used smaller networks with all-to-all coupling to explore population bursting possibilities. Here, our pyramidal models are based on the CA1 region of the hippocampus and even though they also use a simple, one-compartment, Izhikevich-type mathematical structure, they are developed directly from the experimental data (Ferguson et al, 2015). Furthermore, network size and connectivity are directly considered in our models since we have an experimental, network context (see Methods) on which to base our estimates.

The network size and connectivity characteristics are important considerations as they will affect the amount of excitatory interactions, which need to be balanced with the amount of adaptation for the given underlying bursting mechanism. The amount of connectivity between excitatory cells in CA1 and CA3 regions of the hippocampus is quite different with CA3 networks having a higher degree of connectivity (Hasselmo, 2011). Excitatory cells in the CA1 region of hippocampus are minimally connected - less than 1 percent (Bezaire and Soltesz, 2013) - and it might seem unlikely that population bursting could arise in networks with such minimal coupling. In addition to the requirement of a very large network size to consider a physiologically-relevant context (Goutagny et al, 2009), it quickly becomes a huge, computational effort to fully explore parameter ranges in which population bursts (of theta frequency) might occur. To circumvent this, we build on previous mean field theory (MFT) analyses and show that they can reasonably capture simulation results, thus enabling an extensive parameter exploration via MFT to be done, serving as guidance to the full simulations. We also exploit a scaling aspect from the theory to reduce the network size of our simulations and do detailed analyses of network simulations of bursting and spiking characteristics.

In this way we are able to predict the required characteristics for (theta frequency) network bursting to occur in excitatory networks in the CA1 region of hippocampus, identify limitations, and set a balanced framework on which to expand with the addition of inhibitory networks. Our work here can be viewed as an approach for exploration and constraints (and mechanistic understandings) when examining large-scale networks with biologically-based cellular representations.

3.1 MFT and predicting bursting regimes

The primary differences between the network under consideration and previous networks for which mean-field systems have been derived are the Destexhe synapse model and the minimal connectivity. In the following we will show how the mean-field systems shown in the methods section can be modified to take these differences into account.

First we consider the synapse model. Previously derived mean-field systems assumed that the s variable was modelled as a linear synapse. These synapses include the single-exponential, double-exponential, and alpha-synapse (Ermentrout and Terman, 2010). See Methods section for the mean-field model corresponding to a network with double-exponential synapse model. Linear synapses are simpler to average to obtain macroscopic mean-field equations, thus, we will approximate the non-linear Destexhe synapse model given by Eq. (3) with the linear double-exponential synapse model used in Eq. (9). To do this, consider the effect of a single spike at $t = t_0$ on a single synapse:

$$\dot{s} = -\frac{s}{\tau_R} + h \quad (17)$$

$$\dot{h} = -\frac{s}{\tau_D} + \frac{A}{\tau_D \tau_R} \delta(t - t_0) \quad (18)$$

We will approximate the Destexhe synapse by this model by choosing values of the parameters τ_R, τ_D and A to satisfy the following constraints:

1. The Destexhe synapse and the double exponential synapse have the same synaptic rise and decay times.
2. The Destexhe synapse and the double exponential synapse have the same area underneath a pulse

Both these synaptic models have analytical solutions. If a spike occurs at time $t = 0$, then the pulses are given by:

$$E_{Destexhe}(t) = \begin{cases} s_\infty \left(1 - \exp\left(-\frac{t}{\tau_s}\right)\right) & 0 < t < t_1 \\ s_\infty \left(1 - \exp\left(-\frac{t_1}{\tau_s}\right)\right) \exp(-\beta(t - t_1)) & \end{cases} \quad (19)$$

$$E_{Exponential}(t) = \frac{A}{\tau_D - \tau_R} \left(\exp\left(-\frac{t}{\tau_D}\right) - \exp\left(-\frac{t}{\tau_R}\right) \right) \quad (20)$$

where

$$s_\infty = \frac{\alpha T_{max}}{\alpha T_{max} + \beta} \quad \text{and} \quad \tau_s = \frac{1}{\alpha T_{max} + \beta}.$$

Now, it should be clear that the first constraint can be satisfied, when $\tau_R \ll \tau_D$, if we set

$$\tau_R = \tau_s, \quad \tau_D = \frac{1}{\beta}. \quad (21)$$

To force the second constraint, as the area underneath $E_{Exponential}(t)$ is A , then we can merely set A to be the area underneath the Destexhe pulse, which is given by:

$$A = \int_0^\infty E_{Destexhe}(t') dt' = s_\infty \left[t_1 + \left(\frac{1}{\beta} - \tau_s \right) \left(1 - \exp\left(-\frac{t_1}{\tau_s}\right) \right) \right]. \quad (22)$$

Given that we know how to choose A , τ_R and τ_D to force the two constraints, we can see how the Destexhe and double-exponential pulses compare for the parameters values of our model: $T_{max} = 1$, $t_1 = 1$ ms, $\tau_R = 0.5$ ms, $\tau_D = 3$ ms. This is shown in Fig. 1A. The single pulses in Fig. 1A are fairly accurate, however, to be useful, the synapses must perform similarly for more than a single spike. When 5, 50, and 100 Hz background spiking is provided to each synapse, the steady state oscillation for the two synaptic types is similar. See Fig. 1B. However, the similarity breaks down for spiking faster than around 150-200 Hz (not shown). This does not cause a problem for our present study as for the parameter set we are using, spike rates greater than 100 Hz do not occur.

Now we consider how to address the minimal synaptic connectivity. Assuming the probability of two neurons being connected is a Bernoulli random variable, the number of incoming connections to any one neuron is a Binomial distribution with N trials and probability parameter p . In our model the probability of connection between two neurons is small ($p = 0.01$), and the number of neurons is fairly large ($N \sim 10^4$). Given the values of these two parameters, we are well justified in using the normal approximation for N_i , the number of connections coming to neuron i :

$$N_i \sim \mathcal{N}(Np, Np(1-p)) \quad (23)$$

as both Np and $N(1-p)$ are large. This is shown for example in Fig. 1C for a 10,000 neuron model with minimal connectivity of 1%.

As the mean-field systems previously derived assumed all-to-all connectivity, we will need to relate our minimally coupled network to an all-to-all coupled network. Let C be the coupling matrix, i.e., $C_{ij} = 1$ if there is a synapse from neuron j to neuron i otherwise it is 0, and let \bar{g} be the maximal conductance on a single synapse. (So \bar{g} corresponds to g_{pyr}). Then we make the following assumption:

$$\bar{g} \sum_{j=1}^N C_{ij} s_{ij} \approx \bar{g} N_i \frac{1}{N} \sum_{j=1}^N s_{ij} = g_i s_i \approx g_i \langle s \rangle \quad (24)$$

where s_{ij} , s_i , g_i are as described in the Methods. Here $\langle s \rangle$ is the mean s variable derived from all-to-all coupling, as in the previous mean-field models. One may ask whether or not this assumption is justified, as it effectively turns minimal coupling into heterogeneity; $g_i = \bar{g} N_i$ is now a heterogeneous quantity that is approximately distributed as:

$$g_i \sim \mathcal{N}(\bar{g} N p, \bar{g}^2 N p (1-p)). \quad (25)$$

Taking values of N and p such that the approximation (23) is valid, we studied the assumption (24) numerically. We found that it is fairly accurate for parameter values where most of the neurons in the network are spiking/bursting. This shown in Fig. 1D where we compare $\bar{g} \sum_{j=1}^N C_{ij} s_{ij}$ with $\bar{g} N_i \langle s \rangle$ for a two second simulation of a 10,000 neuron network with minimal connectivity of 1%. The assumption is less accurate when there are many neurons which do not spike, i.e., where $\langle I \rangle$ is near rheobase and/or $\sigma_I \geq \langle I \rangle$ (not shown). These parameter regimes are not important for our study as the network either does not burst or the burst frequency is too low.

We now show how this may be further simplified in the appropriate large N limit. We consider p as fixed and such that Np and $N(1-p)$ are both large as $N \rightarrow \infty$. We further assume that the maximal synaptic conductance, \bar{g} , scales as $\frac{1}{N}$, so that in the limit $N \rightarrow \infty$, $\bar{g}Np$ is fixed:

$$\bar{g} \propto \frac{1}{N}, \quad \bar{g}Np \sim g^*, \quad N \rightarrow \infty, \quad (26)$$

which prevents saturation of the network. This in turn implies that in the limit $N \rightarrow \infty$ the normal distribution (25) for g_i tends to:

$$\mathcal{N}(\bar{g}Np, \bar{g}^2Np(1-p)) \sim \delta(g_i - g^*), \quad N \rightarrow \infty$$

Using the fact that as $N \rightarrow \infty$, the heterogeneity we introduced in g becomes narrowly distributed like $1/\sqrt{N}$, we can assume that $\rho_g(g) \sim \delta(g - g^*)$, its asymptotic limit as $N \rightarrow \infty$. In this case, the mean-field system (11)-(15) becomes:

$$\langle u \rangle' = a[b\langle V \rangle - v_r] - \langle u \rangle + d\langle R_i(t) \rangle \quad (27)$$

$$\langle s \rangle' = -\frac{\langle s \rangle}{\tau_R} + \langle h \rangle \quad (28)$$

$$\langle h \rangle' = -\frac{\langle h \rangle}{\tau_D} + \frac{A}{\tau_R \tau_D} \langle R_i(t) \rangle \quad (29)$$

where

$$\langle R_i(t) \rangle = \int_{I^*(\langle u \rangle, \langle s \rangle)}^{\infty} \rho_I(I) \left[\int_{v_{reset}}^{v_{peak}} \frac{C_m}{k(V)(V - v_r)(V - v_t) - \langle u \rangle - g^* \langle s \rangle (V - E_{pyr}) + I} dV \right]^{-1} dI$$

with

$$I^*(\langle u \rangle, \langle s \rangle) = \max_V [-k(V)(V - v_r)(V - v_t) + \langle u \rangle + g^* \langle s \rangle (V - E_{pyr})].$$

Finally, we note that as $b/(kv_r)$ is small enough, we can remove the term $b\langle V \rangle$ from the mean-field system without drastically altering the behavior (Nicola and Campbell, 2013b). **However it can be computed with the mean-field system if necessary.**

We have run this mean-field system with various choices of parameters, and compared it with the network mean adaptation $\langle u \rangle$ and network mean synaptic activity $\langle s \rangle$ computed from simulation of the full network with the same parameters. As shown in Fig. 2, the behaviour of the mean-field system is a good predictor of the behavior of the large network, however, there is error in both the frequency and amplitude of bursting in the mean-field system simulation relative to the full network simulations. The inaccuracy in the frequency is worse at low frequencies in the two dimensional parameter map. Recall that our method of burst frequency calculation is not accurate below 1.4 Hz for 3 second simulations. This inaccuracy can be seen for the simulation associated with Point A. On the parameter map this point is classified as non-bursting, while in the simulation it appears to be bursting with frequency around 1 Hz. It is clear from Fig. 2 that the lower (small $\langle I \rangle$) boundary of the bursting region is associated with low frequency bursting. Thus to determine this boundary with high accuracy would require longer simulations.

While there is noticeable error in both the frequency and amplitude of the mean-field system simulation relative to the full network simulations, this is not critical for the purposes of parameter exploration. The mean-field system is an accurate enough representation of the behaviour of the

network to allow us to use it to predict regions in parameter space that the network will burst. Additionally, the mean-field system gives a reasonably accurate prediction of the bursting frequencies, and is hence useful for studying how the burst frequency changes with respect to the parameters.

The real advantage of this small system of DE's, however, is the simulation time. Using the standard Runge-Kutta integrator in matlab ode45, one can simulate the mean-field system significantly faster (near real time) than an actual network.

3.2 Parameter exploration

With the speed gains we have made with regards to the mean-field system, we do a parameter exploration. As the cellular models were developed directly from experiments in the given experimental context (see Methods), we consider these parameters as fixed (see Table 1). In addition, the synaptic reversal potential is determined in the same experimental context and so is also not varied. From the literature, a range of synaptic conductance values is estimated, as well as values for the synaptic rise and decay, and the amount of connectivity. We therefore focus our parameter exploration on the parameters \bar{g} , $\beta = \frac{1}{\tau_D}$, in addition to the parameters that govern the distribution of applied input current (and hence heterogeneity of the intrinsic neuron firing rates), $\langle I \rangle$ and σ_I . Note that \bar{g} , N and p only appear as the product $g^* = \bar{g}Np$ in the mean-field model. This invariance allows us to study the behaviour as one of \bar{g} , N or p , is varied and then deduce corresponding behaviour for variations in all three parameters. In our study, we vary the parameter \bar{g} , and fix $N = 30,000$ and $p = 0.01$.

We performed our exploration of the four dimensional parameter space as follows. Values of $\bar{g} \in [0, 0.14]$ nS and $\langle I \rangle \in [0, 600]$ pA were chosen from a fine mesh and $\sigma_I \in [0, 80]$ pA and $\tau_D \in [2, 5]$ ms were chosen on a coarser mesh. We note that even though \bar{g} could be much larger and still be within physiological estimates, a much lower upper bound was sufficient to capture the population bursting parameter regimes. We ran **three** second mean-field simulations with each parameter set and computed the predicted burst frequency as described in the Methods. Contour plots of this frequency as a function of \bar{g} and $\langle I \rangle$ were made for each set of σ_I, τ_D values. This is shown in Fig. 3. At a glance, one can see that the maximal population bursts would be predicted to be in the 6-8 Hz frequency range. We can also easily see how the population burst frequency varies with the parameters. With all the other parameters fixed, as \bar{g} increases the frequency of bursting gradually decreases. However, for increasing $\langle I \rangle$ with the other parameters fixed, the burst frequency gradually increases. This agrees with previous work that shows that bursting requires the right balance of synaptic drive (\bar{g}) and external drive ($\langle I \rangle$) (Dur-E-Ahmad et al, 2011). Increasing the synaptic decay time constant has the general effect of moving the bursting region to lower \bar{g} values, while decreasing the burst frequency. This makes sense as increasing τ_D means the cells feel the effect of the synapses longer, so a lower synaptic conductance is needed to achieve bursting. Said another way, increasing τ_D has a similar effect as increasing \bar{g} . Finally, as the amount of heterogeneity increases (i.e., σ_I increases) the bursting region moves to higher \bar{g} and $\langle I \rangle$ values. The interpretation here is that with increasing heterogeneity there are more neurons with external drive too high for their cellular adaptation to be able to contribute to the bursting mechanism and more neurons with external drive too low to be able to spike and be able to contribute to the bursting mechanism. In other words, there may not be a critical mass of neurons which can contribute to the bursting mechanism, and so the network rhythm is lost.

3.3 Scale invariance: Direct comparisons between full simulations and theory

The scaling invariance of the mean-field model carries over to the full networks, but in an approximate way. Recall that g^* is the mean of the distribution of g_i across the network. Thus networks with the same g^* will not be perfectly identical. However, when Np is large we showed above that the distribution becomes more narrowly centered around its mean, hence the scaling invariance should become more accurate. Thus networks that have different values of \bar{g} , N and p should behave similarly if they have the same g^* and Np is suitably large. Given this and the wide parameter exploration done as described in the previous section (see Fig. 3), we can give limits on the parameters for which population bursting can occur. For example, from the $\sigma_I = 15 \text{ pA}$, $\tau_D = 3 \text{ ms}$ plot in Fig. 3, the lowest \bar{g} is about 0.04 nS . Given a 30,000 network size, and considering the physiological range estimate (see Methods), this means that \bar{g} can be as small as 0.008 nS if the connectivity is 5% and population bursting will still occur. Equivalently, the connectivity can be as small as 0.04% if the synaptic strength is 1 nS .

Let us directly examine this theoretical scaling relationship with full simulations. That is, networks with the same g^* where $g^* = \bar{g}Np$, should produce the same output. We perform full simulations in which either the network size or the connectivity is changed, and adjust \bar{g} in the scaling relationship accordingly. Note that in describing the full simulations, we refer to the maximal, excitatory conductances as g_{pyr} and the mean excitatory drive as mean $I_{applied}$ (as given in the Methods) to distinguish from the MFT analyses (which uses \bar{g} and $\langle I \rangle$) In Fig. 4, we show raster plots from simulations using six different network sizes. For comparison and visualization purposes, 1,000 cells are shown in each raster plot regardless of the network size. From these simulations, it is clear that the scaling relationship holds very well, although a network size of 1,000 may be a bit too small for the assumptions in the theoretical analysis to be in effect. In Fig. 5, we show raster plots in which the network size is **held constant at 10,000** and the connectivity is changed. Again, it is clear that the scaling relationship is very robust for these large networks. With this robust scaling, we now focus on 10,000 cell networks (rather than 30,000 as used in the MFT runs of Fig. 3) to consider how our population bursts are affected by changing parameters. We note that with network sizes beyond 10,000, it becomes a bit more challenging to easily simulate the network activity for long periods of time and for many different sets of parameters. Furthermore, to be able to do more detailed analyses of the network simulations (as in the next section), it is important to be able to run simulations for long enough to remove transients and still have enough bursts to do the analyses. Thus, this scaling relationship allows us to be able to have a principled approach in doing parameter explorations in these very large networks.

As described in the previous section, there should be a reasonable match between numerical and MFT results, although the frequencies are not expected to be exactly the same (see Fig. 2). Let us consider an example of a direct comparison between a full 30,000 cell network simulation with parameter values as in Fig. 4 and the MFT using exactly the same parameters. For the full simulation, the burst frequency is close to 2.5 Hz (as estimated from Fig. 4), whereas for the MFT scenario, it is found to be approximately 4.7 Hz (see Fig. 3 - burst frequency value extracted from high resolution MFT plots). Thus, as already noted, there is some error in the predicted frequency. However, the trends when changing parameters are the same as we show below.

A wide range of parameter sets were easily explored using the MFT analysis (Fig. 3). As described above, in the MFT runs we observed a gradual decrease in burst frequencies with increasing

excitatory conductance strengths, and a gradual increase in burst frequencies with increasing excitatory drive. Raster plots from the full simulations are shown in Fig. 6 and Fig. 7 for changing g_{pyr} and changing mean $I_{applied}$ parameter values, respectively. Similar to the MFT runs, we see a decrease in burst frequency with increasing g_{pyr} , and an increase in burst frequency with increasing mean $I_{applied}$. Because of the scaling relationship, we can simply deduce whether the burst frequency would increase or decrease with changing network size and connectivity, given the simulation runs of Fig. 6 without needing to do additional sets of full simulations. That is, if only the connectivity is reduced, the burst frequency would increase, and if only the network size is reduced, the burst frequency would increase. Although the burst frequencies obtained from the theory and from the full simulations differ, the trends are clearly the same so that the parameter balances for which population bursting occurs are well captured by the MFT analyses. As such, the parameter ranges for which full simulations would need to be explored can be significantly reduced. However, the exact boundaries for which population bursts occur would have to be carefully explored with full simulations. We note that in the raster plots of Figs. 4-7, the presence of population bursts is easy to see and they are stable as judged by the extent of the simulation. However, outside of the boundary predicted by the MFT analyses, population bursts that are initially seen are not maintained (i.e., are unstable), so that by the end of the simulation, no population bursts are apparent (not shown).

We previously examined this cellular adaptation bursting mechanism, but with smaller networks and with all-to-all coupling (Dur-E-Ahmad et al, 2011). Here, with much larger networks that are not all-to-all coupled, we find that population bursts can still occur if parameter balances are appropriate. That is, the essential mechanism is still in play. However, now the required balance (to get population bursts) does not only encompass the amount of cellular adaptation and the excitatory drive and synaptic strengths, but also the network size and connectivity (and heterogeneity). Without the theoretical analyses, it would be more difficult and much more time-consuming to determine what parameter balances allow population bursting to emerge. These full simulations already indicate that population bursting can occur using physiologically relevant synaptic conductance values and connectivities found in the CA1 region of hippocampus, but at frequencies on the lower end of theta rhythm. In the next section, we examine a full range of simulations and analyze the cellular spiking and bursting characteristics of the network simulations.

3.4 Network simulation analyses

Given the robust scaling aspect, we do simulations with 10,000 cells rather than with 30,000 cells which would be much more computationally intensive. We carry out simulations for a range of parameters, and perform a detailed analysis of the full simulations to parse out bursting and cellular spiking characteristics. Because of the averaging assumptions in MFT, these additional analyses cannot be obtained from the MFT runs. However, because of the MFT work, we know which parameter sets should be focused on. In this way, we greatly reduce the amount of simulations that need to be done for our analysis.

We focus on g_{pyr} and mean $I_{applied}$ ranges for which a population burst can be easily defined (criteria described in Methods). With this, we can define a burst width and interburst duration, and explore the spiking characteristics during bursting (i.e., within the burst as defined by the burst width) and between bursts. However, because of this, the mean $I_{applied}$ ranges for which bursts are easily defined, are different when using different amounts of heterogeneities (i.e., with different σ_I 's).

This is to be expected as it can be clearly seen from the MFT analyses that the lower boundary for which population bursts occur shifts to larger mean $I_{applied}$ values as the heterogeneity (i.e., σ_I) increases (see Fig. 3).

In Fig. 8 we plot the burst frequency along with the burst duration and interburst durations for four different σ_I values. In comparison with burst frequency changes seen with the MFT (Fig. 3), the trend is the same as expected, and as shown in Fig. 6 and Fig. 7. However, in addition, it is clear from Fig. 8 that the population burst frequency changes that occur when the excitatory conductance strengths or the excitatory drives change are mainly due to changes in the interburst duration (middle column of Fig. 8 - between burst width) and not to changes in the burst duration (right column of Fig. 8 - burst width). Thus, for the cellular adaptation bursting mechanism as described in Dur-E-Ahmad et al (2011), we can say that in these larger networks (that are not all-to-all coupled), the (population) burst frequency is largely controlled by (non-spiking) neuronal processing (between bursts). In other words, since the slowdown in burst frequency occurs due to increasing interburst duration, a key controlling factor for population bursts to emerge is due to spike initiation. That is, the cells' ability to spike again (after the burst ends).

Although we identify spike initiation as a controlling factor in the emergence of population bursts, the underlying mechanism clearly relies on a balance between the amount of cellular adaptation and excitatory coupling. Specifically, the bursting depends on a slow cyclical increase and decrease of adaptation in neurons coupled with the variation in synaptic input. During the active part of the burst, the cells are spiking and the adaptation (represented by the current u_i in our models) increases until it is high enough that the effective input current to the neurons ($I_{applied} - u_i - I_{syn}$) is below rheobase and the neurons cease to spike. This is complicated as $-I_{syn}$ is also increasing as the cell spikes. During the quiescent phase, the cells become uncoupled ($I_{syn} \rightarrow 0$) and the adaptation slowly decays until the effective input current ($I_{applied} - u_i$) goes above rheobase and they begin to spike. In our models $1/a \gg \tau_D \gg \tau_R$ thus the decay rate in the quiescent phase is determined by $1/a$. The width of the quiescent phase is determined by $1/a$ and the difference in the amount of adaptation at the beginning and end $\approx I_{syn} = \bar{g}s(V - E_{pyr})$. There are two key aspects of this mechanism in the homogeneous case. First, the applied current, $I_{applied}$, must be greater than rheobase (in the absence of coupling the cells are tonically firing) so that the network can leave the quiescent phase. Second there must be the right balance of synaptic input and adaptation so that burst termination can occur. However, with heterogeneity and not all-to-all coupling, leaving the quiescent phase and the burst termination depends on the variation of the effective input into all the different cells. As some cells start to spike, they provide other cells (that they are coupled to) with additional input and they in turn can start spiking and have adaptation and so on. The balance is thus dependent on the number of cells and the connectivity also. With the MFT analysis, this overall balance is captured in coming up with the bursting regimes (as in Fig. 3). Thus, spike initiation (of enough cells) is essential, and it is clear that there must be a non-zero number of cells with effective input above rheobase for population bursts to occur.

In Fig. 9 we show how the average spike frequency and the number of cells spiking changes, during bursts and between bursts for a particular level of heterogeneity. It is clear that the average spike frequency increases during the burst more due to increasing g_{pyr} and not due to increasing mean $I_{applied}$. This is consistent across different heterogeneties (not shown). The average spiking frequencies during the burst range from 10-60 Hz for the four different heterogeneties examined ($\sigma_I = 5, 10, 15, 20$ pA), and each cell spikes 1 to 6 times (not shown). It is also very clear that

during bursts, all of the 10,000 cells are spiking for almost the entire range of parameters. Only in small regions of low mean $I_{applied}$ and low g_{pyr} do we find that not all 10,000 cells are spiking. Between bursts, the average spiking frequency is much lower (as expected given the raster plots shown in the earlier figures), with the average number of spikes per cell mostly being less than one (not shown). Also, as can be seen in Fig. 9, this interburst spiking frequency is not sensitive to g_{pyr} at lower mean $I_{applied}$ values, and only a fraction of the cells are spiking between the bursts. Not surprisingly, the number of cells spiking between bursts increases as the heterogeneity increases, but during the burst, it is still the case that all of the cells are spiking (not shown).

3.5 Reduced bursting regimes with weakly adapting excitatory cells

So far, all of the MFT runs and full simulations were done using cellular models that had strongly adapting characteristics. However, as described in the Methods, CA1 pyramidal cells also exhibit weakly adapting characteristics (Ferguson et al, 2015). Using these weakly adapting cellular models, we take advantage of our MFT analysis to easily and quickly examine a full range of parameter sets to see how population bursting regimes change. This is shown in Fig. 10. Given the model mechanism being dependent on adaptation, we expect that with weakly adapting cells, population bursting would be less prevalent relative to networks with strongly adapting cells, as it is. It is also apparent that the burst frequencies are lower. Compare Fig. 3 and Fig. 10, but note that the color ranges encompass different frequency ranges. **In Supplementary Materials, we show the occurrence of population bursts in networks of weakly adapting cells.**

It is clear that while population bursts could still occur in these minimally coupled networks, this behaviour is far less robust than in the networks of strongly adapting neurons. In particular, for fixed values of τ_D and σ_I the region of bursting in the \bar{g} , $\langle I \rangle$ plane is considerably reduced and generally lies at higher \bar{g} and $\langle I \rangle$ values. (Note the change in scale on the \bar{g} axis.) Further, while the effect of varying the parameters is similar to what we observed in the strongly adapting networks, the burst region and burst frequency are more sensitive to variation of these parameters. All this points to the fact that the balance of external and synaptic drive needed to obtain bursting is considerably harder to achieve with weakly adapting neurons. Finally, we note that the achievable range of population burst frequencies is reduced. (Note the change in scale on the bursting frequency colour bar). This is consistent with our other observations as the range of values of \bar{g} and $\langle I \rangle$ where bursting can occur in the weakly adapting network is where the lower bursting frequencies occur in the strongly adapting network.

4 Discussion

Using biologically-based cellular models of CA1 pyramidal cells in hippocampus, we have built large, excitatory networks in an effort to determine whether and how population bursting can emerge. Our models were designed to represent the experimental context of a whole hippocampus preparation that spontaneously exhibits theta frequency (3-12 Hz) population bursts (Goutagny et al, 2009). This population activity was shown to be generated in the CA1 region of the hippocampus, a region where the coupling between excitatory cells is minimal. Taking advantage of mean-field analyses, we were able to examine a very large parameter space. We specifically examined whether

spike frequency adaptation that is present in the individual cells could generate network population bursts, via cellular adaptation mechanisms. The balance between cellular (adaptation) and synaptic (excitatory coupling) characteristics forms the essence of the population bursting mechanism but due to heterogeneity and non all-to-all coupling, the complexity of the balance is greatly increased, but with the mean-field analyses, appropriate parameter regimes are easily found. We found that theta frequency population bursts could emerge but at low theta frequencies (< 4 Hz) in our experimentally-constrained context. Thus, the required balance between the amount of cellular adaptation with excitatory interactions does exist in these excitatory networks, and a controlling aspect of these population bursts lies in spikes being initiated in a non-zero number of cells that have an effective input above their rheobase. As such, we suggest that cellular adaptation mechanisms could be a critical component in the generation of theta frequency population bursts in the hippocampus. It would not be straightforward to directly test our present results as adaptation currents cannot be blocked in isolated and specific ways (e.g., many types of potassium currents could contribute). Furthermore, inhibition is not yet included in the models and some inhibitory cell types are important contributors to the theta rhythm (Amilhon et al, 2015). However, it is interesting to note that population bursts in which inhibitory cells minimally contribute do occur, but these are at frequencies that are lower than theta (Wu et al, 2005). We view the present work as a starting framework on which to build to understand the generation of theta frequency population bursts in the hippocampus. We expect to be able to suggest particular experimental tests when, for example, excitatory-inhibitory networks are considered in this experimental context.

4.1 Relation to our previous modeling work and other considerations

Previously, we developed Izhikevich-based models of pyramidal cells in the CA3 region of the hippocampus (Dur-E-Ahmad et al, 2011). These models were based on data derived from the literature (Hemond et al, 2008) and were designed to capture experimentally recorded spike frequency adaptation characteristics. As in the work here, we were interested to know whether the amount of spike frequency adaptation that is present in biological cells would be appropriate to support population bursting in hippocampal networks. That work was focused on CA3 cells because of related experimental studies that showed a population bursting pattern (*in vitro* sharp wave) initiating in the CA3 region of the hippocampus (Wu et al, 2005). That work showed that it was possible that adaptation characteristics as estimated from experimental records could support network bursting. However, in that work, the cellular characteristics were not derived directly from experiment, and the network constraints in terms of size and connectivity were not directly considered – smaller networks and only all-to-all coupling was used. In the work here, our network models are well-defined in terms of experimental context: the cellular models were developed in the same experimental context with direct experimental data (Ferguson et al, 2015), and the network size was based on estimates from the experimental preparation exhibiting spontaneous theta rhythms (Goutagny et al, 2009). We note that although our cellular models still use an Izhikevich model structure as in Dur-E-Ahmad et al (2011), we consider them as biologically-based as the parameters were chosen to match characteristics such as frequency-current profiles and rheobases, but not biophysically-based as they do not have conductance representations like Hodgkin-Huxley types. Even though there are other choices one could make for these simple models (Gerstner and Brette, 2009), the Izhikevich type works well enough and is amenable for robust simulations of very large networks.

The network models considered here only include excitatory networks, and although we found that robust, theta frequency population bursts could occur, they were at lower theta frequencies for networks composed of strongly adapting cells (Fig.3 and Fig.8). When only weakly adapting cells were used in the excitatory networks, the regions in which population bursts could occur were reduced and population burst frequencies were much lower, and no longer in the theta frequency range (Fig.10). We focused our detailed network simulation analyses on the strongly adapting excitatory cell networks. Relative to what is known about the experimental data, the most obvious discrepancy between model and experiment is the lack of sparse firing in the models that is present in the experimental data (Huh et al, 2015). The full simulations showed that except for a small regime at low values of g_{pyr} and mean $I_{applied}$, all of the cells are spiking during the population burst (see Fig. 9). In preliminary work, we have found that with the addition of inhibitory cells, sparse firing of excitatory cells can occur at the same time as robust population bursts (Ferguson et al, 2014).

An important aspect to consider is the amount of input (i.e., excitatory drive) that is needed for population bursts to emerge. For our strongly adapting cell models, the rheobase is 0 pA, so that with a mean $I_{applied}$ greater than zero in our network simulations, more than 50% of the cells in the network are above rheobase and would spike intrinsically. Interestingly, earlier work by Latham et al (2000) showed that an essential aspect needed for rhythmic bursting is a non-zero fraction of endogenously active cells (as demonstrated in model and experiment in their scenario). **Future studies of excitatory and inhibitory cell networks building on the starting network framework here may be able to estimate the required amount of endogenously firing cells for the emergence of theta frequency population bursts.**

In a previous modeling study we built networks to capture population activities from normal and Rett mouse models (as given by MeCP2-null mice) (Ho et al, 2014). To do this, we took advantage of cellular adaptation mechanisms in the excitatory network models. In earlier modeling work we had found that model inhibitory networks underlying the normal population activities were mainly controlled by excitatory fluctuations, rather than (tonic) excitatory drive (Ho et al, 2012). We translated this interpretation to excitatory networks with different amounts of heterogeneity (via the σ_I parameter) in Ho et al (2014) – Rett model output occurring when the excitatory fluctuations were smaller (interpreted as smaller heterogeneity). The model Rett (excitatory) networks (with smaller heterogeneity) exhibited population bursting at lower excitatory conductance strengths relative to the normal networks. From our work here, it is clear that this is to be expected now that we are able to see the wide range of parameter sets easily obtained from the MFT runs (see Fig. 3). With all parameters fixed except for the amount of heterogeneity, the boundary of where population bursts first appear occurs at higher excitatory conductance values as σ_I increases.

Ideally, one should use noisy (and not heterogeneous) input with linkage to experimental measurements. While we have done a linkage with experiment in previous work (Ho et al, 2009), it can become quite challenging due to technical extraction issues from the experimental data. From a modeling viewpoint, we do not expect that our essential network results would change if noisy rather than heterogeneous input were used, based on our previous simulation studies of inhibitory networks using heterogeneous (Ferguson et al, 2013) or noisy input (Skinner and Ferguson, 2013) and our mean-field studies of all-to-all, excitatory networks with noise (Nicola et al, 2014). However, the essential issue is being able to have interpretations for the model parameters relative to experiment so that insight into the biological system can be gained.

4.2 Theoretical aspects and relation to our other studies

In the work here, we extended our mean-field derivation to deal with two new aspects: Destexhe (kinetic) synapse model and minimal connectivity. To our knowledge this is the first time that mean-field models have been derived for networks with these properties. The Destexhe kinetic model was dealt with by approximating it using the double exponential model for which the mean field derivation has been done. This approximation is valid so long as the activation time constant of the synapse is sufficiently faster than that of the inactivation time constant - they differ by an order of magnitude in the work here so this approximation is very good. To deal with minimal connectivity we considered an asymptotic limit as the number of neurons in the network gets large $N \rightarrow \infty$. Assuming that the probability, p , of two neurons being connected is such that both Np and $N(1-p)$ are large we showed that the number of connections coming into a given neuron obeys a normal distribution. **We then made an assumption (valid if most of the neurons in the network are spiking/bursting) so that we could treat minimal connectivity as heterogeneity in the maximal synaptic conductance.** Making the final assumption that the maximal synaptic conductance scales as $1/N$, we showed that for N sufficiently large the mean-field for the minimally coupled network with maximal synaptic conductance \bar{g} is well approximated by that for an all-to-all coupled network with maximal synaptic conductance $g^* = \bar{g}Np$. This also showed that there is a scaling relation for the mean-field systems. Any two systems with the same g^* will have similar behaviour.

Our previous theoretical studies of all-to-all coupled networks showed that heterogeneity in applied current can lead to sparse firing (Nicola and Campbell, 2013b). In particular, sparse firing occurred in a small region where \bar{g} and $\langle I \rangle$ are both low and the size of the region of sparse firing increased with σ_I . In this work, all the neurons receive the same excitatory drive due to the all-to-all coupling. Thus the sparse firing must arise due to the heterogeneity in $I_{applied}$. With small enough $\langle I \rangle$ the total drive of many neurons falls below rheobase and the neuron does not fire. With a large $\langle I \rangle$ many neurons have $I_{applied}$ high enough that the spike frequency adaptation is not strong enough for bursting to emerge (i.e., the neurons are tonically firing). A $\langle I \rangle$ low enough such that some neurons have strong enough spike frequency adaptation is needed for the population burst to emerge. If \bar{g} is too small, many neurons may have total input below rheobase and do not fire so do not participate in the burst. As \bar{g} increases, the number of neurons participating in bursts increases. Interestingly, the sparse firing region seemed to be associated with the parameter values where the Hopf bifurcation associated with the emergence of bursting is supercritical. Where the Hopf is subcritical the whole network seems to transition to bursting at the same parameter values.

Here we showed that bursting is much harder to achieve in networks of weakly adapting neurons than strongly adapting neurons. This is consistent with our previous work on all-to-all coupled networks (Nicola and Campbell, 2013b). In that work we considered a case study of a population containing both strongly adapting and weakly adapting neurons. We showed that the higher the proportion of weakly adapting neurons in the network the smaller the set of $\langle I \rangle$ and \bar{g} values for which the network would burst.

One factor we have left out of our network models is noise. It is possible to derive mean-field systems for network with noise (Nicola et al, 2014; Nesse et al, 2008). The overall results are similar, with a region of bursting existing in the $\bar{g}, \langle I \rangle$ parameter space. Notably, this region can extend below rheobase and as the strength of the noise increases the bursting regions moves to lower values of $\langle I \rangle$ and large values of \bar{g} . We did not study sparse firing explicitly, but the noise can cause the

appearance of a supercritical Hopf bifurcation, thus it seems likely that small regions will occur as in the case of heterogeneity in $I_{applied}$.

4.3 Related Studies

Work by Augustin et al (2013) is similar to ours in that adaptation-based bursting is considered with simple two-variable neuron models and mean-field analyses. However, the examination is generic with excitatory/inhibitory networks, synaptic delays and spike frequency adaptation, and not focused on a particular brain region with experimentally constrained cellular models. **We have focussed on adaptation induced bursting in the CA1 region of hippocampus. Similar studies have been done focussing on other regions and other mechanisms for population bursting. For example, Tabak et al (2000); Vladimirov et al (2008) studied bursting in chick spinal chord induced by slow synaptic depression. Further, Butera et al (1999a,b) studied in network bursting in the Pre-Botzinger complex. They primarily focus on the role of intrinsically bursting cells in producing population rhythms, showing that only a small fraction of pace-maker cells is needed even in minimally coupled networks.** For us, one of the main goals of the theoretical MFT work was to guide the simulations, as we could easily do a much more expansive parameter exploration in the MFT model, in particular where the experimental constraints were limited. However, several experimental constraints were clear as our model networks were designed and developed using the whole hippocampus experimental preparation spontaneously expressing theta rhythms. The MFT analyses here achieved a close correspondence with the full simulations. We have focussed on bursting as a mechanism for producing network theta rhythms. Other authors have focussed on clustering as a means of producing population rhythms. Kilpatrick and Ermentrout (2011) looked at how spike frequency adaptation was related to clustering in excitatory/inhibitory networks the emergence of higher gamma (30-100 Hz) frequencies, while a focussed role of inhibition in a similar vein was done by Krupa et al (2014).

4.4 Concluding remarks

By taking an approach in which theoretical, modeling and experimental aspects are considered together at early stages we have been able to take advantage of MFT analyses to quickly do expansive parameter explorations to guide full network simulations. Importantly, these simulations are of cellular-based network models that were developed using a well-defined experimental context. In this way, it should be possible to go back and forth between model and experiment to identify critical aspects contributing to biologically-based mechanisms in the generation of population rhythms in the hippocampus. At this stage, our network models are focused on excitatory networks, but this work constitutes a framework on which we will build by the addition of inhibitory networks, including inhibitory cells of different types.

Figure Captions

Fig. 1

Numerical verification of the main approximations used to derive the mean-field model.

(a) Comparison of simulations of the synaptic response to a single spike using the Destexhe model (red) and the double exponential model (black). The parameters of the double exponential synapse are set to reproduce both the rise and decay times and the area under the curve generated by the Destexhe synapse. (b) Same as (a) except the stimulus is a 100 Hz train of spikes. (c) A network model of 10,000 neurons with minimal connectivity was set up as follows. The nonzero elements of the connection matrix were set randomly, with the probability of a connection between any two neurons being 1%. The number of connections to each neuron was then computed and a probability density function for the number of connections was estimated by applying a kernel density estimator to the data. This estimated pdf is shown in blue, while the normal approximation, $\mathcal{N}(Np, Np(1-p))$, is shown in red. (d) The network described in (b) was simulated for 2 seconds. The value of $g_i(t) = \bar{g} \sum_{j=1}^N C_{ij} s_{ij}$, is compared to the approximation $\bar{g} N_i \langle s \rangle$ for five randomly chosen neurons.

Fig. 2

Mean-field accuracy.

Top. The mean-field system described in the text was simulated for 3 seconds using values for the parameters \bar{g} and $\langle I \rangle$ taken from a 40×40 mesh on $[0, 0.3] \times [0, 600]$ with $\sigma_I = 5$ pA and $\tau_D = 3$ ms. The burst frequency is computed at each mesh point as described in the Methods.

Middle and Bottom. Simulations of the mean-field system (red) are compared with those of a network of 10,000 neurons with 1% connectivity (blue) for four representative parameter sets.

Fig. 3

MFT Parameter Exploration with strongly adapting cell networks.

The mean-field system, with strongly adapting single cell parameter values from Table 1, was simulated for a 3 second time interval using values for the parameters g and $\langle I \rangle$ taken from a 30×30 mesh over the ranges shown on the plot with $\sigma_I = 0, 5, 10, 15, 20, 40, 80$ pA and $\tau_D = 2, 3, 4, 5$ ms. The burst frequency at each mesh point is computed as described in the Methods.

Fig. 4

Scaling Relationship - changing network size.

Raster plots of six different network sizes are shown for 2 seconds of simulation. Note that each plot shows 1,000 cells regardless of the network size.

Parameter values are (left to right, top to bottom): 1,000 neurons, $g_{pyr}=1.425$ nS; 5,000 neurons, $g_{pyr}=0.2850$ nS; 10,000 neurons, $g_{pyr}=0.1425$ nS; 20,000 neurons, $g_{pyr}=0.0713$ nS; 25,000 neurons, $g_{pyr}=0.0570$ nS; 30,000 neurons, $g_{pyr}=0.0475$ nS. In all cases there is 1% connectivity and $\sigma_I = 15$ pA, mean $I_{applied} = 80$ pA, $\tau_D = 3$ ms.

Fig. 5

Scaling Relationship - changing connectivity.

Raster plots of three different network connectivities are shown for 4 seconds of simulation with transients removed. Each raster plot shows 1,000 of the 10,000 cells in the network. Parameter

values are: (top) 0.5% connectivity, $g_{pyr}=0.2850$ nS; (middle) 1% connectivity, $g_{pyr}=0.1425$ nS; (bottom) 2% connectivity, $g_{pyr}=0.0713$ nS. In all cases there are 10,000 cells in the network with $\sigma_I = 15$ pA, mean $I_{applied} = 80$ pA, $\tau_D = 3$ ms.

Fig. 6
Increasing burst frequency with decreasing excitatory strength.

Raster plots of three network with different excitatory strengths are shown for 5 seconds of simulation with transients removed. Parameter values are: (top) $g_{pyr}=0.1425$ nS; (middle) $g_{pyr}=0.1155$ nS; (bottom) $g_{pyr}=0.1020$ nS. In all cases there are 10,000 cells in the network with 1% connectivity and $\sigma_I = 5$ pA, mean $I_{applied} = 20$ pA, $\tau_D = 3$ ms.

Fig. 7
Increasing burst frequency with increasing excitatory drive.

Raster plots of three network with different excitatory drives are shown for 5 seconds of simulation with transients removed. Parameter values are: (top) mean $I_{applied}=20$ pA; (middle) mean $I_{applied}=40$ pA; (bottom) mean $I_{applied}=60$ pA. In all cases there are 10,000 cells in the network with 1% connectivity and $\sigma_I = 5$ pA, $g_{pyr} = 0.1290$ nS, $\tau_D = 3$ ms.

Fig. 8
Burst frequency changes due to interburst interval changes.

First column shows the burst frequencies (Hz), second column shows the interburst durations or the width between bursts (ms), and third column shown the burst widths or durations (ms). $\sigma_I = 5, 10, 15, 20$ pA (top to bottom). Note that mean $I_{applied}$ ranges from 40-100 pA to allow for consistency for all σ_I values. Color ranges adjusted to be the same for all σ_I values, but note that the time duration range for the interburst intervals are not the same as for the burst width ranges. It is much narrower for the burst widths.

Fig. 9
Cellular spiking characteristics.

Average spike frequencies and the number of spiking cells are shown for the time between bursts (first column) and during bursts (second column). Note that the mean $I_{applied}$ ranges are from 10-100 pA, which is wider than the mean $I_{applied}$ range shown in Fig. 8, as only $\sigma_I = 5$ pA is shown. Note that the color ranges for between and during bursts are different as the spike frequency and number of spiking cells is much higher during the bursts.

Fig. 10
MFT Parameter Exploration with weakly adapting cell networks.

The mean-field system, with weakly adapting single cell parameter values from Table 1, was simulated for a 3 second time interval using values for the parameters g and $\langle I \rangle$ taken from a 30×30 mesh over $[0, 0.15] \times [0, 600]$ with $\sigma_I = 0, 5, 10, 15, 20, 40$ pA and $\tau_D = 2, 3, 4, 5$ ms. The burst frequency at each mesh point is computed as described in the Methods. Note that color ranges are not the same as for strongly adapting networks shown in Fig. 3.

Supplementary Materials

Figure S1

Weakly Adapting Networks

Raster plots showing population bursting in networks of weakly adapting cells. An example of an individual cell firings is also shown. Parameter values: (top left) mean $I_{applied}=150$ pA, $g_{pyr} = 0.22$ nS; (bottom left) example of an individual cell firing from the above raster plot; (top right) mean $I_{applied}=175$ pA, $g_{pyr} = 0.22$ nS; (bottom right) mean $I_{applied}=300$ pA, $g_{pyr} = 0.36$ nS; In all cases there are 10,000 cells in the network with 1% connectivity and $\sigma_I = 5$ pA, $\tau_D = 3$ ms.

References

- Abbott LF, van Vreeswijk C (1993) Asynchronous states in networks of pulse-coupled oscillators. *Physical Review E* 48:1483–1490
- Amilhon B, Huh CL, Manseau F, Ducharme G, Nichol H, Adamantidis A, Williams S (2015) Parvalbumin Interneurons of Hippocampus Tune Population Activity at Theta Frequency. *Neuron* 86(5):1277–1289, DOI 10.1016/j.neuron.2015.05.027
- Apfalter F, Ly C, Tranchina D (2006) Population density methods for stochastic neurons with realistic synaptic kinetics: Firing rate dynamics and fast computational methods. *Network: Computation in Neural Systems* 17:373–418
- Augustin M, Ladenbauer J, Obermayer K (2013) How adaptation shapes spike rate oscillations in recurrent neuronal networks. *Frontiers in Computational Neuroscience* 7:9, DOI 10.3389/fncom.2013.00009
- Battaglia FP, Benchenane K, Sirota A, Pennartz CM, Wiener SI (2011) The hippocampus: hub of brain network communication for memory. *Trends in Cognitive Sciences* 15(7):310–318, DOI 10.1016/j.tics.2011.05.008
- Bezaire MJ, Soltesz I (2013) Quantitative assessment of CA1 local circuits: Knowledge base for interneuron-pyramidal cell connectivity. *Hippocampus* DOI 10.1002/hipo.22141
- Brette R, Gerstner W (2005) Adaptive exponential integrate-and-fire model as an effective description of neuronal activity. *Journal of Neurophysiology* 94(5):3637–3642
- Butera R, Rinzel J, Smith J (1999a) Models of respiratory rhythm generation in pre-Bötzinger complex. I. Bursting pacemaker neurons. *Journal of Neurophysiology* 81:382–397
- Butera R, Rinzel J, Smith J (1999b) Models of respiratory rhythm generation in pre-Bötzinger complex. II. Populations of coupled pacemaker neurons. *Journal of Neurophysiology* 81:398–415
- Buzsaki G (2011) Hippocampus. *Scholarpedia* 6(1):1468, DOI 10.4249/scholarpedia.1468
- Destexhe A, Mainen Z, Sejnowski T (1994) An efficient method for computing synaptic conductances based on a kinetic model of receptor binding. *Neural Computation* 6:14–18
- Deuchars J, Thomson A (1996) CA1 pyramid-pyramid connections in rat hippocampus in vitro: Dual intracellular recordings with biocytin filling. *Neuroscience* 74(4):1009–1018, DOI 10.1016/0306-4522(96)00251-5
- Dur-E-Ahmad M, Nicola W, Campbell SA, Skinner FK (2011) Network bursting using experimentally constrained single compartment CA3 hippocampal neuron models with adaptation. *Journal of Computational Neuroscience* DOI 10.1007/s10827-011-0372-6
- Ermentrout GB, Terman DH (2010) *Mathematical Foundations of Neuroscience*. Springer, New York
- Ferguson K, Huh C, Amilhon B, Williams S, Skinner F (2014) Parvalbumin-positive interneurons play a key role in determining the frequency and power of CA1 theta oscillations in experimentally constrained network models, program No. 303.22. 2014 Neuroscience Meeting Planner. Washington, DC: Society for Neuroscience, 2014. Online.
- Ferguson KA, Huh CYL, Amilhon B, Williams S, Skinner FK (2013) Experimentally constrained CA1 fast-firing parvalbumin-positive interneuron network models exhibit sharp transitions into coherent high frequency rhythms. *Frontiers in Computational Neuroscience* 7:144, DOI 10.3389/fncom.2013.00144
- Ferguson KA, Huh CYL, Amilhon B, Williams S, Skinner FK (2015) Simple, biologically-constrained CA1 pyramidal cell models using an intact, whole hippocampus context. *F1000Research* 3:104 DOI [v2;refstatus:indexed,http://f1000r.es/5fu]10.12688/f1000research.

- 3894.2
- Gerstner W, Brette R (2009) Adaptive exponential integrate-and-fire model. *Scholarpedia* 4(6):8427
- Goodman DFM, Brette R (2009) The Brian simulator. *Frontiers in Neuroscience* 3, DOI 10.3389/neuro.01.026.2009
- Goutagny R, Jackson J, Williams S (2009) Self-generated theta oscillations in the hippocampus. *Nature Neuroscience* 12(12):1491–1493, DOI 10.1038/nn.2440
- Gutkin B, Zeldenrust F (2014) Spike frequency adaptation. *Scholarpedia* 9(2):30,643
- Hansel D, Mato G (2001) Existence and stability of persistent states in large neuronal networks. *Physical Review Letters* 86(18):4175
- Hansel D, Mato G (2003) Asynchronous states and the emergence of synchrony in large networks of interacting excitatory and inhibitory neurons. *Neural Computation* 15:1–56
- Hasselmo M (2011) Models of hippocampus. *Scholarpedia* 6(5):1371, DOI 10.4249/scholarpedia.1371
- Hemond P, Epstein D, Boley A, Migliore M, Ascoli GA, Jaffe DB (2008) Distinct classes of pyramidal cells exhibit mutually exclusive firing patterns in hippocampal area CA3b. *Hippocampus* 18(4):411–424, DOI 10.1002/hipo.20404
- Ho ECY, Zhang L, Skinner FK (2009) Inhibition dominates in shaping spontaneous CA3 hippocampal network activities in vitro. *Hippocampus* 19(2):152–165, DOI 10.1002/hipo.20493
- Ho ECY, Strber M, Bartos M, Zhang L, Skinner FK (2012) Inhibitory Networks of Fast-Spiking Interneurons Generate Slow Population Activities due to Excitatory Fluctuations and Network Multistability. *The Journal of Neuroscience* 32(29):9931–9946, DOI 10.1523/JNEUROSCI.5446-11.2012
- Ho ECY, Eubanks JH, Zhang L, Skinner FK (2014) Network models predict that reduced excitatory fluctuations can give rise to hippocampal network hyper-excitability in MeCP2-null mice. *PLoS ONE* 9(3):e91,148
- Huh C, Amilhon B, Ferguson K, Torres-Platas S, Manseau F, Peach J, Scodras S, Mechawar N, Skinner F, Williams S (2015) Excitatory inputs determine phase-locking strength and spike-timing of CA1 stratum oriens/alveus parvalbumin and somatostatin interneurons during intrinsically generated hippocampal theta rhythm, In Revision
- Izhikevich EM (2003) Simple model of spiking neurons. *IEEE transactions on neural networks* 14(6):1569–1572, DOI 10.1109/TNN.2003.820440
- Kilpatrick ZP, Ermentrout B (2011) Sparse gamma rhythms arising through clustering in adapting neuronal networks. *PLoS Comput Biol* 7(11):e1002,281, DOI 10.1371/journal.pcbi.1002281
- Knight BW (2000) Dynamics of encoding in neuron populations: some general mathematical features. *Neural Computation* 12:473–518
- Krupa M, Gielen S, Gutkin B (2014) Adaptation and shunting inhibition leads to pyramidal/interneuron gamma with sparse firing of pyramidal cells. *Journal of Computational Neuroscience* 37(2):357–376, DOI 10.1007/s10827-014-0508-6
- Latham PE, Richmond BJ, Nelson PG, Nirenberg S (2000) Intrinsic dynamics in neuronal networks. I. Theory. *Journal of Neurophysiology* 83(2):808–827
- Lisman JE (1997) Bursts as a unit of neural information: making unreliable synapses reliable. *Trends in Neurosciences* 20(1):38–43
- Loken C, Gruner D, Groer L, Peltier R, Bunn N, Craig M, Henriques T, Dempsey J, Yu CH, Chen J, Dursi J, Chong J, Northrup S, Pinto J, Knecht N, Van Zon R (2010) Scinet: Lessons learned from building a power-efficient top-20 system and data centre. *Journal of Physics: Conference Series* 256:012,026

- 1
2
3
4
5
6
7
8
9
10
11
12
13
14
15
16
17
18
19
20
21
22
23
24
25
26
27
28
29
30
31
32
33
34
35
36
37
38
39
40
41
42
43
44
45
46
47
48
49
50
51
52
53
54
55
56
57
58
59
60
61
62
63
64
65
- Ly C, Tranchina D (2007) Critical analysis of dimension reduction by a moment closure method in a population density approach to neural network modeling. *Neural Computation* 19:2032–2092
- Nesse WH, Borisyuk A, Bressloff P (2008) Fluctuation-driven rhythmogenesis in an excitatory neuronal network with slow adaptation. *Journal of Computational Neuroscience* 25:317–333
- Nicola W, Campbell SA (2013a) Bifurcations of large networks of two-dimensional integrate and fire neurons. *Journal of Computational Neuroscience* 35(1):87–108, DOI 10.1007/s10827-013-0442-z
- Nicola W, Campbell SA (2013b) Mean-field models for heterogeneous networks of two-dimensional integrate and fire neurons. *Frontiers in Computational Neuroscience* 7:184, DOI 10.3389/fncom.2013.00184
- Nicola W, Ly C, Campbell SA (2014) One-dimensional population density approaches to recurrently coupled networks of neurons with noise, arXiv:1408.4767
- Skinner FK (2012) Cellular-based modeling of oscillatory dynamics in brain networks. *Current opinion in neurobiology* 22(4):660–669, DOI 10.1016/j.conb.2012.02.001
- Skinner FK, Ferguson KA (2013) Modeling oscillatory dynamics in brain microcircuits as a way to help uncover neurological disease mechanisms: A proposal. *Chaos: An Interdisciplinary Journal of Nonlinear Science* 23(4):046,108, DOI 10.1063/1.4829620
- Spruston N, Jonas P, Sakmann B (1995) Dendritic glutamate receptor channels in rat hippocampal CA3 and CA1 pyramidal neurons. *The Journal of Physiology* 482 (Pt 2):325–352
- Tabak J, Senn W, O’Donovan MJ, Rinzel J (2000) Modeling of spontaneous activity in developing spinal cord using activity-dependent depression in an excitatory network. *The Journal of Neuroscience* 20(8):3041–3056
- Tóth K (2010) Glutamatergic neurotransmission in the hippocampus. In: Cutsuridis V, Graham B, Cobb S, Vida I (eds) *Hippocampal Microcircuits*, Springer Series in Computational Neuroscience, Springer New York, pp 99–128
- Touboul J (2008) Bifurcation analysis of a general class of nonlinear integrate-and-fire neurons. *SIAM Journal on Applied Mathematics* 68(4):1045–1079
- Vladimirski B, Tabak J, O’Donovan M, Rinzel J (2008) Episodic activity in a heterogeneous excitatory network, from spiking neurons to mean field. *Journal of Computational Neuroscience* 25:39–63
- van Vreeswijk C, Hansel D (2001) Patterns of synchrony in neural networks with spike adaptation. *Neural Computation* 13(5):959–992
- Wu C, Asl MN, Gillis J, Skinner FK, Zhang L (2005) An in vitro model of hippocampal sharp waves: regional initiation and intracellular correlates. *Journal of Neurophysiology* 94(1):741–753, DOI 10.1152/jn.00086.2005
- Yoder N (2014) PeakFinder: Noise tolerant fast peak finding algorithm, <http://www.mathworks.com/matlabcentral/fileexchange/25500-peakfinder>

1
2
3
4
5
6
7
8
9
10
11
12
13
14
15
16
17
18
19
20
21
22
23
24
25
26
27
28
29
30
31
32
33
34
35
36
37
38
39
40
41
42
43
44
45
46
47
48
49
50
51
52
53
54
55
56
57
58
59
60
61
62
63
64
65

List of Tables

1 Pyramidal Cell Model Parameters 29

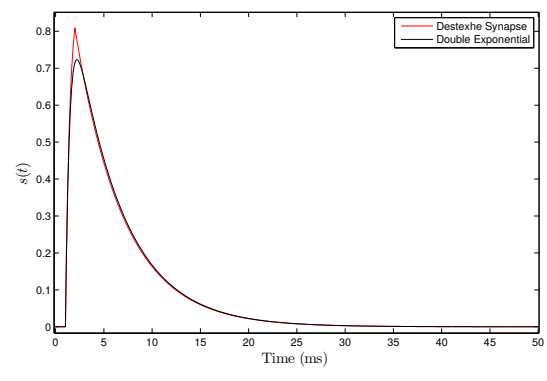
Table 1 Pyramidal Cell Model Parameters

Parameter	PYR	
	weakly adapting	strongly adapting
v_r (mV)	-61.8	-61.8
v_t (mV)	-57.0	-57.0
v_{peak} (mV)	22.6	22.6
a (ms^{-1})	0.00008	0.0012
b (nS)	3	3
c (mV)	-65.8	-65.8
d (pA)	5	10
k_{low} (nS/mV)	0.5	0.1
k_{high} (nS/mV)	3.3	3.3
C_m (pF)	300	115
I_{shift} (pA)	-45	0

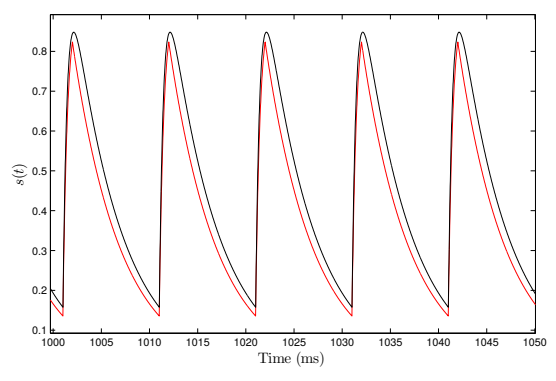
Figure 1

[Click here to download Figure: Fig1.eps](#)

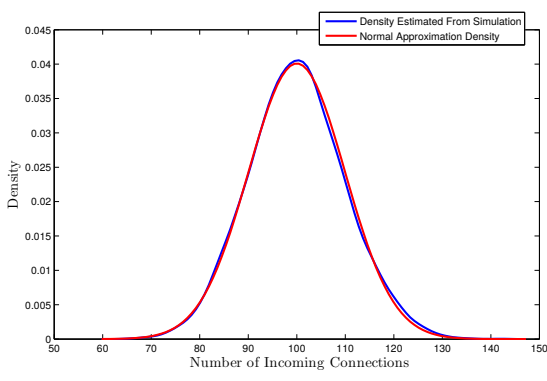
FIGURE 1



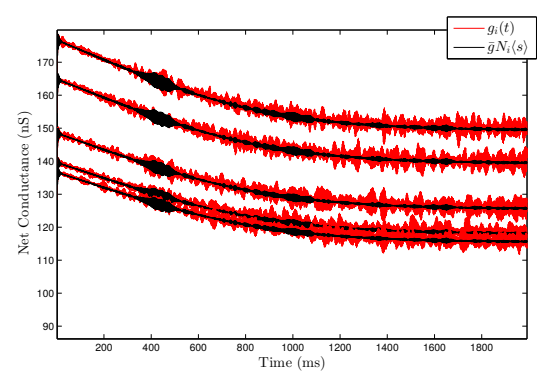
(a) Synaptic models - single pulse



(b) Synaptic models - 100 Hz stimulus



(c) Density of incoming connections



(d) $g_i(t)$ vs. $\bar{g}N_i\langle s \rangle$

Figure 2

[Click here to download Figure: Fig2.eps](#)

FIGURE 2

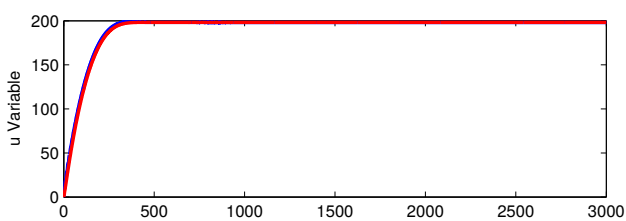
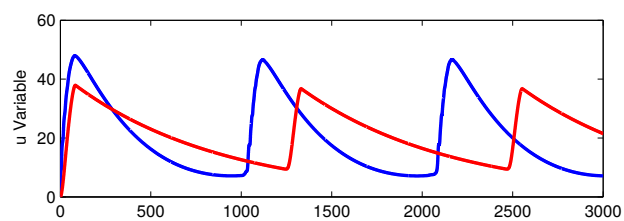
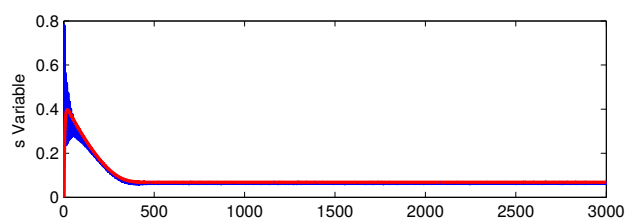
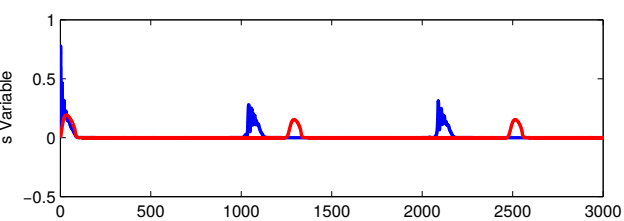
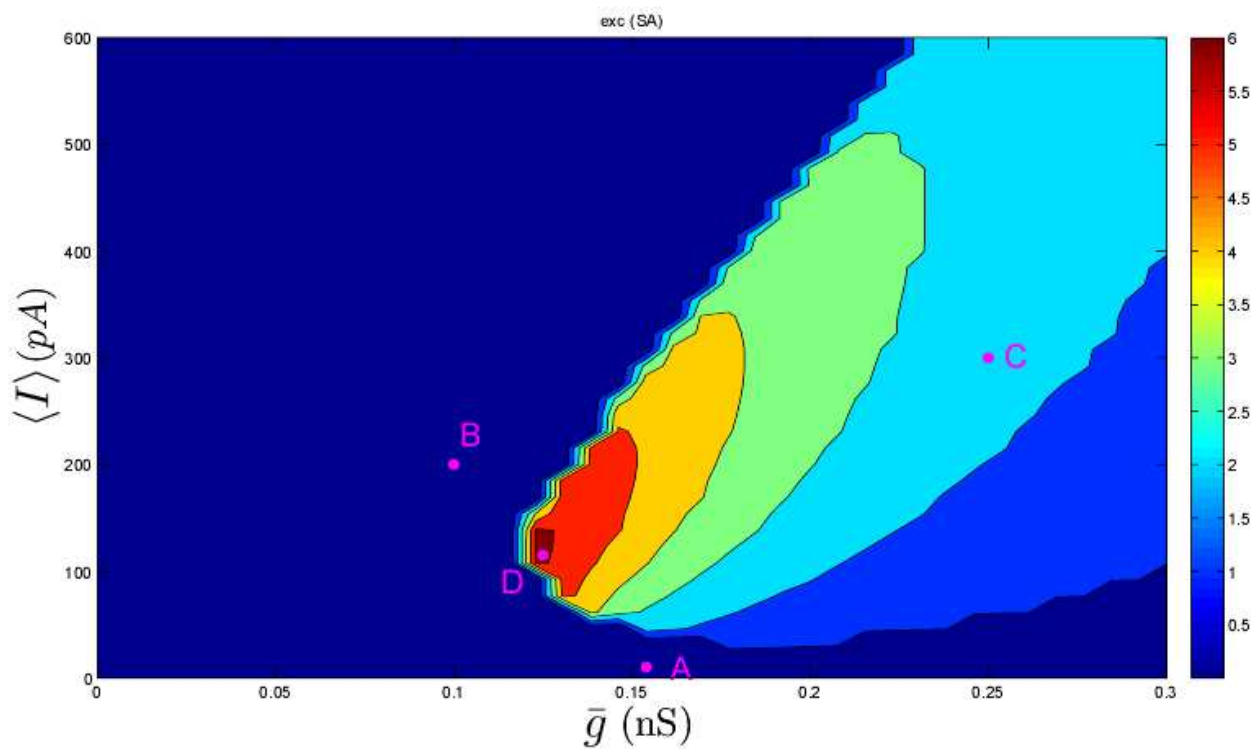
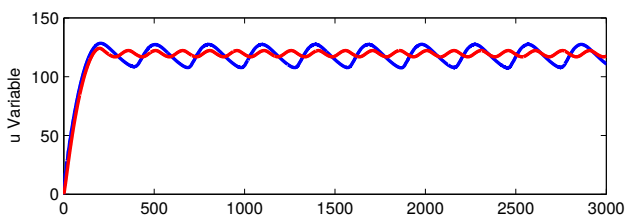
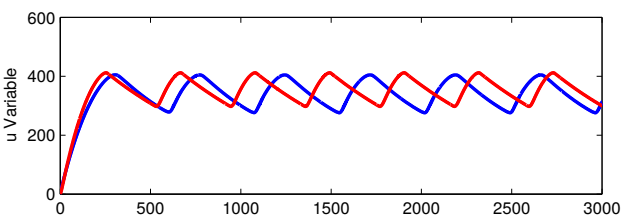
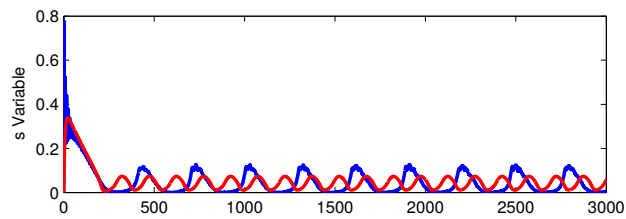
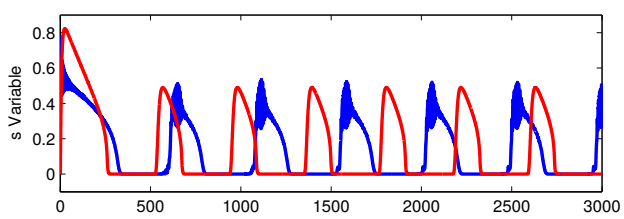
Point A: $\bar{g} = 0.15$ nS, $\langle I \rangle = 10$ pAPoint B: $\bar{g} = 0.1$ nS, $\langle I \rangle = 200$ pAPoint C: $\bar{g} = 0.25$ nS, $\langle I \rangle = 300$ pAPoint D: $\bar{g} = 0.13$ nS, $\langle I \rangle = 110$ pA

Figure 3
[Click here to download Figure: Fig3.tif](#)

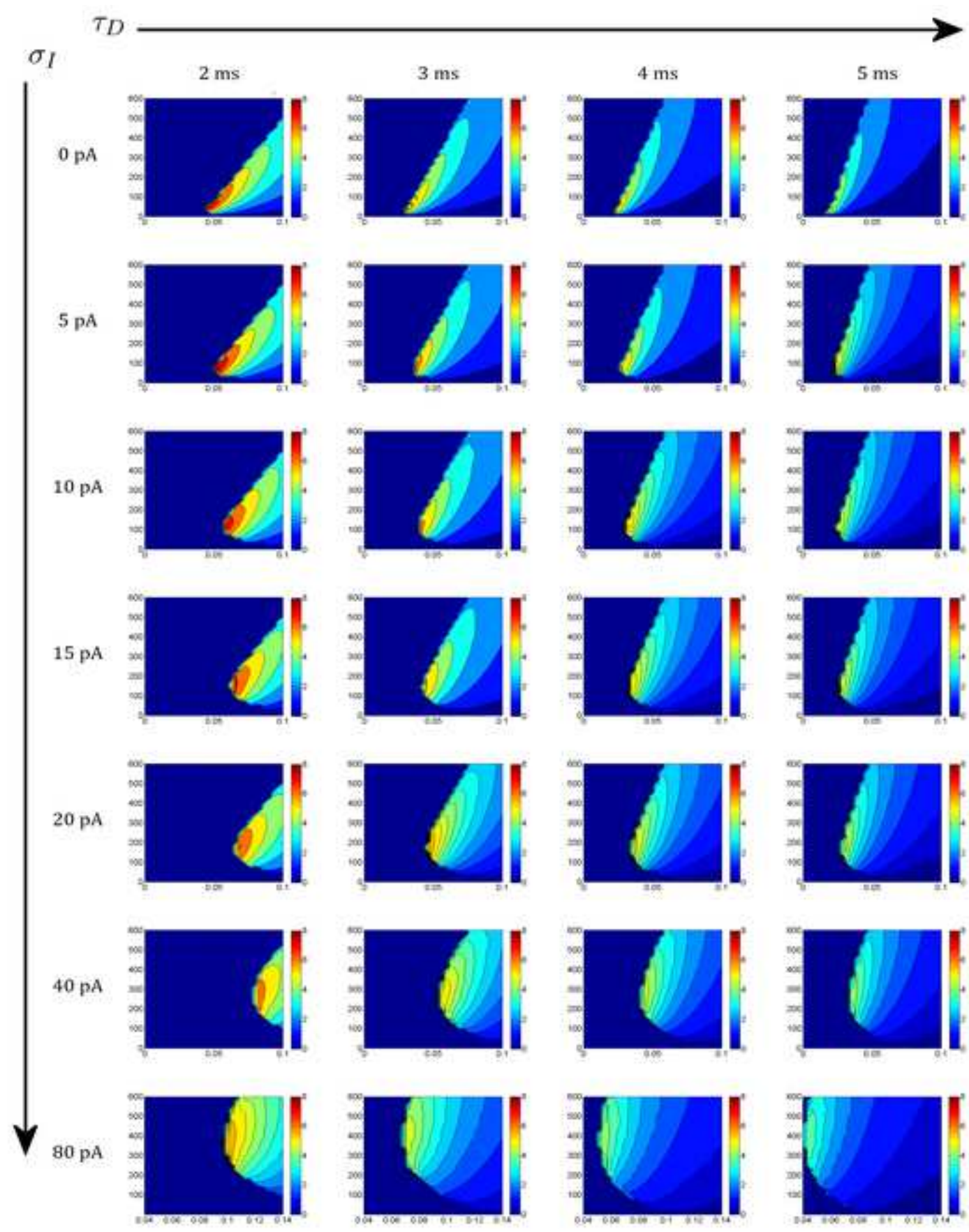


Figure 4
[Click here to download Figure: Fig4.tiff](#)

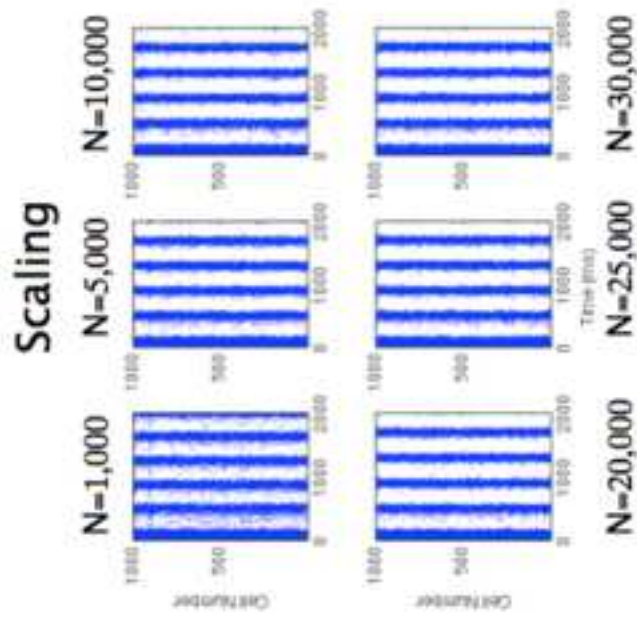


Figure 5
[Click here to download Figure: Fig5.tiff](#)

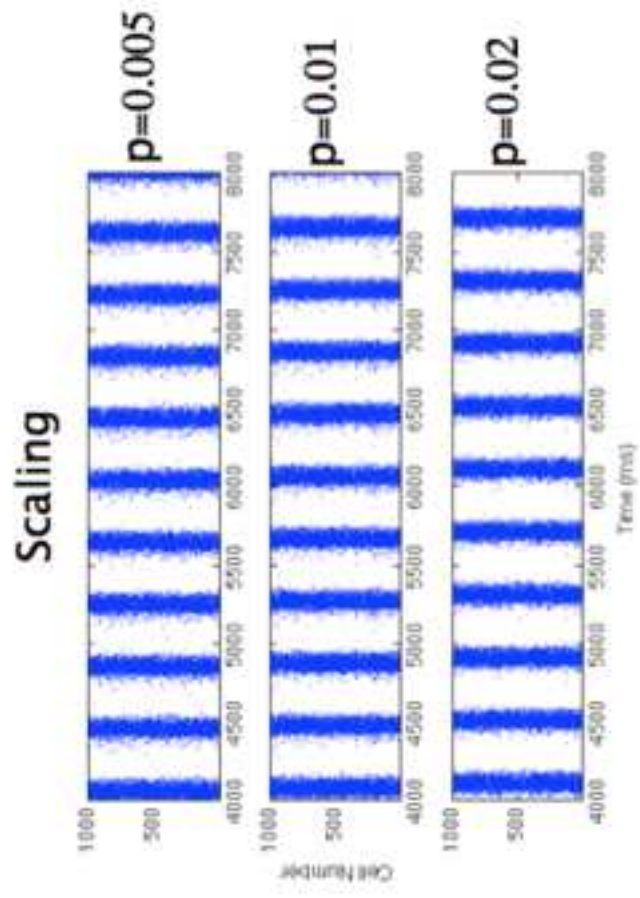


Figure 6
[Click here to download Figure: Fig6.tiff](#)

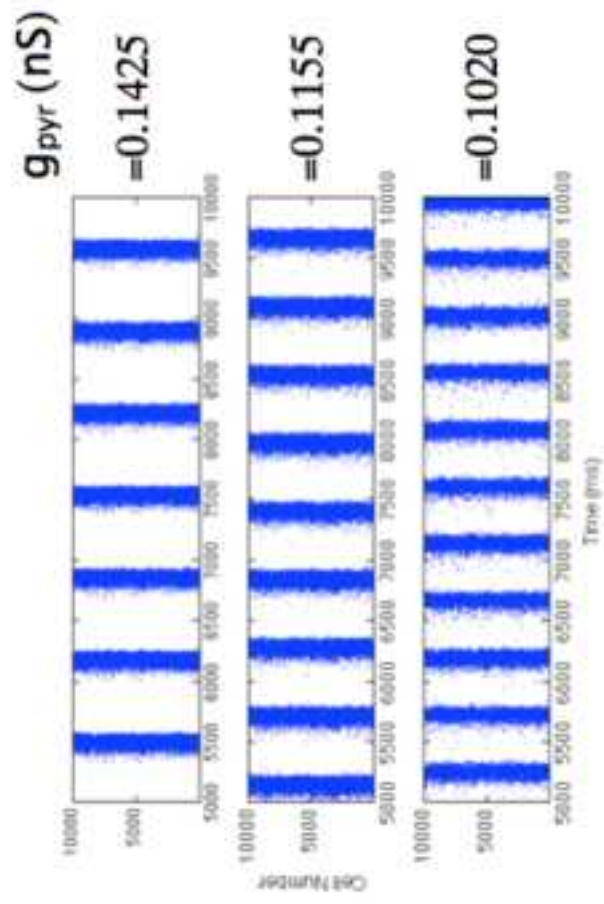


Figure 7
[Click here to download Figure: Fig7.tiff](#)

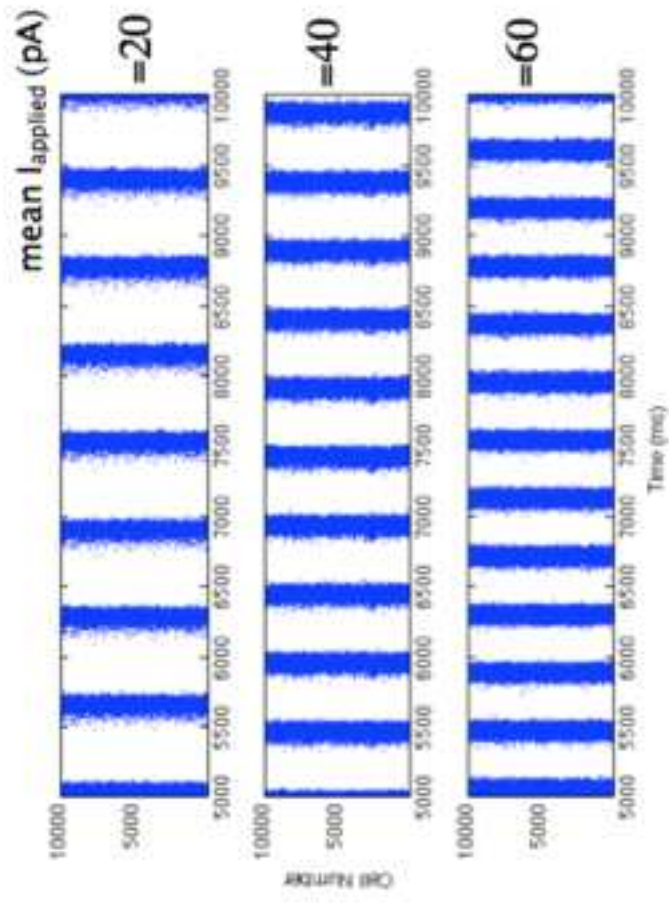


Figure 8
[Click here to download Figure: Fig8.tiff](#)

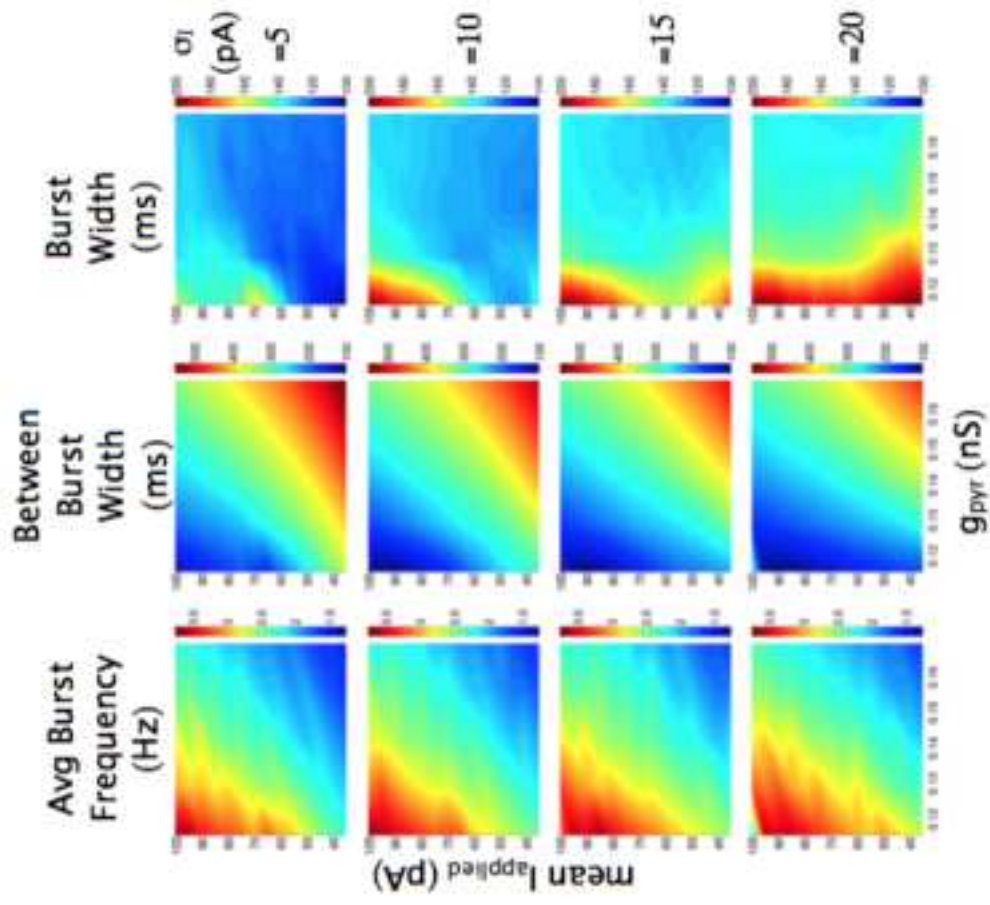


Figure 9
[Click here to download Figure: Fig9.tiff](#)

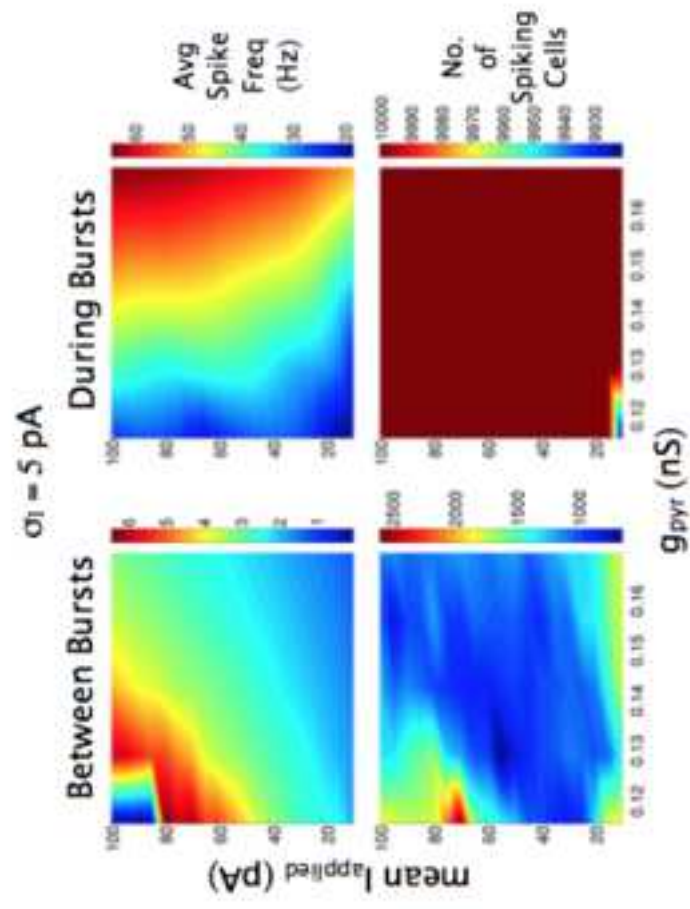


Figure 10
[Click here to download Figure: Fig10.tif](#)

